

AD-A083 394

NAVAL RESEARCH LAB WASHINGTON DC
CASE STUDIES OF FATIGUE CRACK GROWTH USING AN IMPROVED MICRO-LI--ETC(U)
JAN 80 J M KRAFFT

F/0 11/6

UNCLASSIFIED

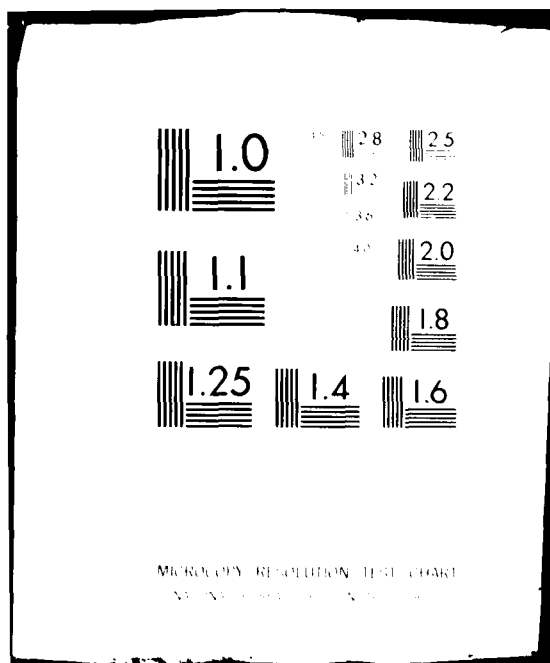
NRL-MR-4161

SBIE-AD-E000 392

NL

| OF |
AD
A083394

END
DATE FILMED
5-80
DTIC



MICROSCOPY RESOLUTION TEST CHART
Nikon Instruments Inc., Melville, NY

12
NW LEVEL III

AD-E000 392

NRL Memorandum Report 4161

Case Studies of Fatigue Crack
Growth Using An Improved Micro-Ligament
Instability Model

J. M. KRAFFT

Ocean Technology Division
Naval Research Laboratory

AM 083304

January 30, 1980

DTIC
ELECTED
APR 24 1980
S D
B



NAVAL RESEARCH LABORATORY
Washington, D.C.

Approved for public release; distribution unlimited.

DMC FILE COPY

80 3 3 079

SECURITY CLASSIFICATION OF THIS PAGE (When Data Entered)

REPORT DOCUMENTATION PAGE		READ INSTRUCTIONS BEFORE COMPLETING FORM
1. REPORT NUMBER NRL Memorandum Report 4161	2. GOVT ACCESSION NO.	3. RECIPIENT'S CATALOG NUMBER
4. TITLE (and Subtitle) CASE STUDIES OF FATIGUE CRACK GROWTH USING AN IMPROVED MICRO-LIGAMENT INSTABILITY MODEL		5. TYPE OF REPORT & PERIOD COVERED Interim report on a continuing NRL problem
7. AUTHOR(s) J.M. Kraft		6. PERFORMING ORG. REPORT NUMBER
9. PERFORMING ORGANIZATION NAME AND ADDRESS Naval Research Laboratory Washington, D.C. 20375		10. PROGRAM ELEMENT, PROJECT, TASK AREA & WORK UNIT NUMBERS 84-0263-0-0; RR023-03-45 84-0264-0-0; WR022-01-01
11. CONTROLLING OFFICE NAME AND ADDRESS Naval Research Laboratory Washington, D.C. 20375		12. REPORT DATE January 30, 1980
		13. NUMBER OF PAGES 70
14. MONITORING AGENCY NAME & ADDRESS (if different from Controlling Office)		15. SECURITY CLASS. (of this report) Unclassified
		15a. DECLASSIFICATION/DOWNGRADING SCHEDULE
16. DISTRIBUTION STATEMENT (of this Report) Approved for public release; distribution unlimited.		
17. DISTRIBUTION STATEMENT (of the abstract entered in Block 20, if different from Report)		
18. SUPPLEMENTARY NOTES		
<p style="text-align: right;">DTIC ELECTE S APR 24 1980 D</p> <p style="text-align: right;">B</p>		
19. KEY WORDS (Continue on reverse side if necessary and identify by block number) Fatigue Crack Propagation Corrosion Fatigue Fatigue Propagation Model Plastic Flow to Fracture Relationships		
20. ABSTRACT (Continue on reverse side if necessary and identify by block number) The tensile ligament instability model TLIM has been refined and modified. A large set of new data cases is analyzed using the improved algorithm, most of these with high fidelity. In micro-structurally varied titanium alloys, the process zone size is associated with the effective grain size; in structural and alloy steels it decreases with increasing yield strength, presumably here too related to grain refinement. The other fitting parameters, of environmental surface attack, show an internal consistency among the various specimen materials and environments. The modified model is thought to provide an advantageous means of comparing crack propagation data, and, in selected classes of materials, a suitable basis for predicting fatigue propagation life.		

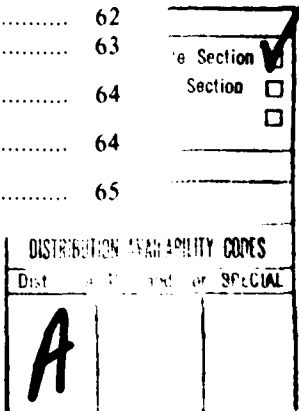
DD FORM 1 JAN 73 1473 EDITION OF 1 NOV 68 IS OBSOLETE
S/N 0102-014-6601

SECURITY CLASSIFICATION OF THIS PAGE (When Data Entered)

~~PRECEDING PAGE BLANK - NOT FILMED~~

CONTENTS

1. INTRODUCTION	1
2. MODELING EQUATIONS	2
2.1 Limited Tensile Instability	3
2.2 Crack-Tip Straining	3
2.3 Specifics for the Growth Rate Equation	4
2.4 Curves of Time- and of Strain-Limited Surface Attack	6
2.5 Corresponding K-strain Excursion	8
2.6 Modification of Earlier TLIM Algorithm	9
3. PREPARING OF GRF PARAMETRIC CURVES	11
3.1 Measuring Stress/Strain/Time Curves	11
3.2 Reading and Correcting Flow Data	12
3.3 Pairing Monotonic with Cyclic Properties vs Strain Excursion	16
3.4 Pairing Monotonic and Cyclic Properties vs Δ K-strain	16
3.5 Plotting Growth Rate Factors Maps	17
3.6 Installing Matching Guidelines	17
3.7 Number of Fitting Parameters	18
4. CASE STUDIES	19
4.1 Iron Based Alloys	21
4.2 Titanium Based Alloys	36
4.3 Aluminum Base Alloys	48
5. COMPARISON OF FITTING PARAMETERS	51
5.1 Trends in Process Zone Size	51
5.2 Trends in Frequency-Independent Parameters	56
5.3 Trends in Frequency-Dependent Parameters	57
6. DISCUSSION	59
6.1 Sources of Correlation Errors	59
6.2 d_T vs Microstructural Sizes	60
6.3 d_T from Low Temperature K_{fc} (K) Matchings	60
6.4 Cleavage in FCGR Prediction	61
6.5 Yield Strength Effect on K_{TH} ; on K_k	62
6.6 Strain Rate Effects	63
7. CONCLUSION	64
ACKNOWLEDGMENTS	64
REFERENCES	65



CASE STUDIES OF FATIGUE CRACK GROWTH USING AN IMPROVED MICRO-LIGAMENT INSTABILITY MODEL

1. INTRODUCTION

A current emphasis of the crack propagation phase of fatigue failure is justified in several ways. It is seen to underlie estimates of air-frame structural integrity and damage tolerance. The fatigue stress allowables of welded structures, such as offshore oil recovery platforms and pipelines, appear to be largely governed by crack propagation life. The ASME pressure vessel code utilizes crack propagation rate data for assessing the hazard of positive NDT indications. Even in aircraft jet engine parts retired on reaching a given probability of small-crack initiation, the remaining propagation life is of interest in assessing the hazard of emergency excess hours without inspection, or the risk of continued use of overaged parts which pass inspection.

Fatigue propagation life of a structure is best measured by direct simulation of its loading spectrum. However, it is less costly to estimate this from steady-state data, modified by suitable overload retardation models. Even here, the cost and time required to develop sufficient data can be burdensome. A goal of propagation modeling is to reduce this burden. With physically based models, an additional benefit could be an enhanced understanding of microstructural and environmental effects.

As with previous NRL reports on this endeavor [1,2,3,4], this one puts forth modeling refinements that evolved in attempting additional data analyses. In the present set, 29 combinations of composition and heat treatment of alloys, comprising 116 variations of conditions of load ratio, frequency, and environment, are analyzed. Some 75% of these materials are newly

Manuscript submitted December 10, 1979

J. M. KRAFFT

reported here: the rest re-analyzed to provide a more complete set. Except for one major modification affecting stage II R-effects, the present model is essentially as that detailed in Ref. [4]. Accordingly this report presents only essential steps of the derivation, which has been reduced to a simpler, more direct form than before.

It should be stated at the outset that the development to follow here is not a rigorous analysis of the elastic-plastic crack tip field nor of the micro-separation processes which reside in it. It is rather a refined dimensional analysis, combining simple limiting solutions of these problems in a manner that permits correlation of a large body of experimental data. Success at correlation is only circumstantial evidence of proper combinations. However, while awaiting more rigorous solutions, this approach is thought to provide useful insights, and even predictive capabilities, otherwise unavailable.

2. MODELING EQUATIONS

This model explores the proposition that stability of crack propagation requires, more essentially than other things, maintenance of a state of constant-load stability within a material-specific region very close to the crack tip. For simplicity of modeling, it considers the material in this region to be formed into tiny cylindrical tensile ligaments, which are extended by the external loading as well as by the consequent stable propagation of the crack. As any specimen subjected to tensile strain, strain-hardening enhances stability, while Poisson contraction reduces it. Two other agents of instability are germane. Firstly, when active straining ceases at the crack tip during the dwell time of cyclic loading, stress relaxation can reduce ligament load bearing capacity, hence stability. This is a volume effect which, except for bulk diffusion processes, should be independent of the environment. Secondly, because the ligament is so small, environmental attack can cause a significant reduction of its effective area, hence load

capacity. Such attack can be considered, in the manner of corrosion processes, as a surface effect limited by exposure time up to a saturation condition. It may be limited, alternatively, by insufficient surface-disturbing plastic strain due to crack loading and propagation.

2.1 Limited Tensile Instability

Consider a simple tensile specimen of sectional area A , subjected to load P , for which true stress σ is defined

$$\sigma = P/A; \quad P = \sigma A; \quad dP = \sigma dA + Ad\sigma \quad (1)$$

A condition verging on tensile instability is $dP = 0$, at a load maximum, for which Eq. (1) becomes

$$\sigma dA = -Ad\sigma \quad (2)$$

To replace the total differentials of area and stress, on a ligament of radius $r_T = d_T/2$, the following partials are germane:

$$\partial A_v = -2\nu\pi r_T^2 d\epsilon; \quad \partial A_s = -2\pi r_T dr_T \quad (3)$$

$$\partial\sigma_\theta = \theta d\epsilon; \quad \partial\sigma_m = -m\sigma dt/t \quad (4)$$

Here ν is the Poisson ratio, ϵ is strain, θ is the strain hardening rate ($d\sigma/d\epsilon$), m is the stress relaxation exponent and t is time. Combining these in Eq. (2) and solving for $d\epsilon$

$$d\epsilon = \left[2 \frac{dr_T}{r_T} + m \frac{dt}{t} \right] \left(\frac{\theta}{\sigma} - 1 \right)^{-1} \quad (5)$$

2.2 Crack-Tip Straining

In Eq. (5), $d\epsilon$ may be regarded as the strain differential required to maintain the constant load condition, $dP = 0$. An expression for how such strain derives from the loading and growth of the crack is needed. This model employs the simplest of crack tip plasticity models, the analogue of the linear elastic stress field, providing an inverse half power singularity

strength near the crack tip. It is employed provisionally, as, for materials of ordinary strain hardening exponents, several analyses have indicated stronger than half power singularities. However, use of this weakest possible singularity seems to provide closer data correlations, in conjunction with other assumptions of this model algorithm. The analogue used is

$$\sigma_y = K_I / \sqrt{2\pi r}; \epsilon = K_I / \sqrt{2\pi r} E \quad (6)$$

whence differentiating

$$d\epsilon = \left(r^{-1/2} dK - \frac{K}{2} r^{-3/2} dr \right) / \sqrt{2\pi} E \quad (7)$$

where K_I is the opening mode stress intensity factor, r is distance ahead of the crack, and E is Young's modulus. Let $r = d_T$, $dr = -da$ where a is crack length, then

$$d\epsilon = d\epsilon_L + \frac{\epsilon_G}{4r_T} da \quad (8)$$

Here $d\epsilon_L$ designates a strain differential due to crack loading, while ϵ_G a strain associated with the strain gradient $d\epsilon/dr$, hence $-d\epsilon/da$, at the point $r = d_T$. Since we need be concerned with maintaining stability only after the loading has ceased in the fatigue cycle, we neglect $d\epsilon_L$ in substituting Eq. (8) in Eq. (5), yielding

$$da = \left(8dr_T + 4m r_T \frac{dt}{t} \right) \left[\epsilon_G \left(\frac{\theta}{\sigma} - 1 \right) \right]^{-1} \quad (9)$$

2.3 Specifics for the Growth Rate Equation

The general crack growth relationship, Eq. (9), shows that the principal impediment to crack growth is the strain hardening rate of the material. Ordinary and cyclic strain hardening characteristics differ markedly. Both are involved in some way at the crack tip in fatigue. Cyclic loading produces cyclic straining at the crack tip. Yet if there is substantial growth during the period of sustained load, the crack may invade material of virgin characteristics, unaffected by the cycling. After trials of many correlation algorithms, the option chosen is to

NRL MEMORANDUM REPORT 4161

divide the effects decisively on the basis of limiting cases of crack propagation, namely: to associate cyclic strain hardening, a function of the strain excursion, with the impedance of stress-relaxation induced growth; and to associate monotonic strain hardening, a function of the maximum strain, with impedance of environmentally induced growth. This defines two distinct forms of the square-bracketed last term of Eq. (9), called a growth rate factor G

$$G_1 \equiv \left[\epsilon_1 \left(\frac{\theta_{1p}}{\sigma_1} - \frac{\sqrt{3}}{2} \right) \right]^{-1} \quad (10)$$

and

$$G_2 \equiv \left[\epsilon_2 \left(\frac{\theta_{2p}}{\sigma_2} - \frac{\sqrt{3}}{2} \right) \right]^{-1} \quad (11)$$

In the foregoing, θ_{1p} and θ_{2p} are plastic-only strain hardening rates, $\theta_p^{-1} = \theta^{-1} - E^{-1}$, corresponding to the plastic strain dependency of the stress relaxation and the work hardening processes. Here the monotonic stress σ_1 is as measured from a zero stress origin, and converted to true stress. However the cyclic stress is the positive excursion of a cyclic loop in balance with its negative excursion, as disposed in a centroid-neutralized equilibrium position, as justified in Ref. [5]. The term $\sqrt{3}/2$, slightly less than unity, can be justified as a plane strain triaxiality effect on the instability condition [6]. It has the effect of increasing the point of terminal instability in a way helpful in correlating materials with very flat monotonic stress-strain curves. With this growth partition hypothesis, Eq. (9) can be expressed as

$$da = 4 r_T m G_2 dt/t + 8 G_1 dr_T \quad (12A)$$

It is helpful at this point to express the crack growth as a finite increment in a cycle of crack loading, and corresponding ligament straining. Consider loading from K_{\min} to K_{\max} in an interval t_L , and thence holding on K_{\max} for an interval t_H . With this, Eq. (12) can be expressed, assuming the change in r_T to be relatively small

$$\Delta a = 4 r_T m \ln(1 + t_H/t_L) G_2 + 8 \Delta r_T G_1 \quad (12B)$$

or abbreviated

$$\Delta a = f_2 G_2 + f_1 G_1 \quad (12C)$$

Here incremental steps approximate the differentials. A summed or averaged growth rate factor may be defined as

$$GRF = \Delta a / f_2 = G_2 + \frac{f_1}{f_2} G_1 \quad (13)$$

In this paper we have used a single value for the loading wave form factor, $\ln(1 + t_H/t_L) = 0.3$ (vs 0.4 in Ref. [4]). This value is used to fit data for both sinusoidal and triangular wave forms used in the FCGR tests. With this value, Eq. (13) can be restated

$$GRF = \frac{\Delta a}{1.2mr_T} = G_2 + \left[\frac{\Delta r_T}{r_T} \right] G_1 / 0.15 m \quad (14)$$

2.4 Curves of Time- and of Strain-Limited Surface Attack

The two ways of limiting surface attack in the fatigue cycle were noted earlier. The effect of varying these limits is displayed by two families of curves. One is a family of curves for a parametric set of constant values of r_T -normalized surface attack intrusion, $[\Delta r_T/r_T]$; the second is a set for such intrusion relative to the total plastic tensile strain on the d_T -ligament during one loading cycle, $[\Delta r_T/r_t/\Delta\epsilon]$. Identifying the family members in best fit to the CFCG data, sets the value of the fitting parameters, other than r_T .

For the first family, Eq. (14) is restated

$$GRF = G_2 + [\Delta r_T/r_T] G_1 / 0.15 m \quad (15)$$

or for the parametric N-family

$$G(N) = G_2 + [2^N] G_1 / 0.15 m \quad (16)$$

The crack growth rate is thus

$$\left(\frac{da}{dN} \right)_t = 1.2 m r_T G(N) \quad (17)$$

For the second family, Eq. (14) is restated

$$GRF = G_2 + \Delta\epsilon \left[\frac{\Delta r_T/r_T}{\Delta\epsilon} \right] G_1/0.15 m \quad (18)$$

Here the $\Delta\epsilon$ term is intended to include plastic strain due to both the loading and propagation of the crack, as in Eq. (8), approximated here in incremental form, with Eq. (14) substituted for Δa

$$\Delta\epsilon = \Delta\epsilon_L + 0.3 m \epsilon_G GRF \quad (19)$$

The loading (plastic) strain $\Delta\epsilon_L$ is associated with the total strain of the cyclic stress strain curve, less its elastic strain

$$\Delta\epsilon_L = \epsilon_{2p} = \epsilon_2 - 2\sigma_2/E_2 \quad (20)$$

Estimating the propagation strain is not so neat, as the amount of propagation depends on the value of GRF, the variable being solved for. Considering the term $0.3 m \epsilon_G GRF$, it is not clear what to use for ϵ_G since, in effect, ϵ_2 was used for it in the G_2 term of GRF , while ϵ_1 was used in the G_1 term. Corresponding values of this differ at non-zero stress ratio, as detailed later. To obtain a closed-form solution, only one can be used. In this case, the gradient strain is set equal to the maximum strain, corresponding to its value in G_1 . This is the more accurate value in regions where the G_1 term dominates the G_2 term, as is the typical of higher strength materials of high environmental sensitivity. For softer, less sensitive materials, the propagation paths are dominated by the G_2 term itself, rather than $G(M)$. Here this inaccuracy in $G(M)$ is unimportant. With this approximation, then, Eq. (18) becomes

$$GRF = G_2 + \left[\epsilon_2 - \frac{2\sigma_2}{E_2} + \epsilon_1 0.3 m GRF \right] \left[\frac{\Delta r_T/r_T}{\Delta\epsilon} \right] G_1/0.15 m \quad (21)$$

Solving for GRF then

$$GRF = \frac{G_2 + \left[\frac{\Delta r_T/r_T}{\Delta\epsilon} \right] \epsilon_1 G_1/0.15 m}{1 - \left[\frac{\Delta r_T/r_T}{\Delta\epsilon} \right] 2 G_1} \quad (22)$$

or for the parametric M-family

$$G(M) = \frac{G_2 + [2^M] \epsilon_1 G_1 / 0.15 m}{1 - [2^M] 2 G_1} \quad (23)$$

Similarly to Eq. (17), the crack growth rate for this family is simply

$$\left(\frac{da}{dN} \right)_\epsilon = 1.2 m r_T G(M) \quad (24)$$

2.5 Corresponding K-strain Excursion

Effects of load ratio R on the values of G_1 and G_2 are considered next. If the load ratio is zero and crack tip strain is proportional to the stress intensity factor, then total elastic plus plastic strains of measurement in the two cycles can be compared directly. However, if R is greater than zero, then one associates monotonic properties, hence G_1 , with a strain larger than that for cyclic properties, hence G_2 . If the strain excursion is taken as a base, as is ΔK , then the basis of association is

$$\Delta\epsilon = \epsilon_2 = (1 - R) \epsilon_1 \quad (25)$$

This means that to calculate a GRF for a given value of strain excursion $\Delta\epsilon$, one uses cyclic properties at strain $\epsilon_2 = \Delta\epsilon$ to compute G_2 , while using monotonic properties at strain $\epsilon_1 = \Delta\epsilon/(1-R)$ to compute the corresponding value of G_1 .

What level of stress intensity factor excursion ΔK is required to effect this strain $\Delta\epsilon$ at d_T ? The model allows for a slight degree of ineffectiveness, or slack, in coupling the overall K-excursion to the strain excursion at the crack tip. This slack is analogous to the crack closure concept of Elber [7]. The amount of this slack is taken as one-half the monotonic tensile yield point strain, from an argument viewing the compressive stress-strain quadrant as "off limits" for the cyclic strain excursion for positive stress ratios [4]. This "closure strain", $\epsilon_{CL} = TYS/2E$, is taken as a fixed augmentation of the monotonic form of $\Delta\epsilon$ in Eq. (25). In the cyclic form, it

is added only to the extent that the minimum strain $R \Delta\epsilon/(1-R)$ is less than the closure strain, or the difference greater than zero. Normally this term vanishes for R values greater than about 0.3. With this, the ΔK -proportional strain is defined

$$\Delta\epsilon_K = \Delta\epsilon + \epsilon_{CL} \quad (26)$$

$$= \epsilon_2 + [\epsilon_{CL} - R \epsilon_2/(1 - R)]_{>0} \quad (27)$$

$$= (1 - R) \epsilon_1 + \epsilon_{CL} \quad (28)$$

The cyclic excursion ΔK may now be defined after Eq. (6) for the point $r = d_T = 2 r_T$

$$\Delta K = \sqrt{4\pi r_T E} \Delta\epsilon_K. \quad (29)$$

An illustration of foregoing considerations is attempted in Fig. 1.

2.6 Modification of Earlier TLIM Algorithm

This model differs from that of Ref. [4] and Ref. [9] in one major respect, as well as in several minor ones. The major change is that the gradient strain in G_1 , Eq. (10) and in $G(M)$, Eq. (21), is taken as a maximum strain rather than a strain excursion. When the strain excursion is used here, the level of $G(N)$, at the constant N fitting a stage II corrosion fatigue growth, rises with stress ratio. The Bucci* data on Ti-8-1-1 in salt water appeared to exhibit this. However, when this is applied to Vosikovsky data on X70 steel and to Ritchie data on 300M, the R-effect appears erroneous. It is now believed that the increasing growth rates of the Ti-8-1-1 data should be associated with a loading in which K_{min} exceeds K_{Iscc} , which is Bucci's explanation of this effect. With high stress ratio, this occurs at relatively low ΔK levels, as shown later.

The numerous minor changes are to be noted. In Ref. [4], a cyclic stress value was used in calculating G_1 as well G_2 . The gradient strain values were put in as K -strains ϵ_K and $\Delta\epsilon_K$,

*References to authors' works noted in the section are cited later.

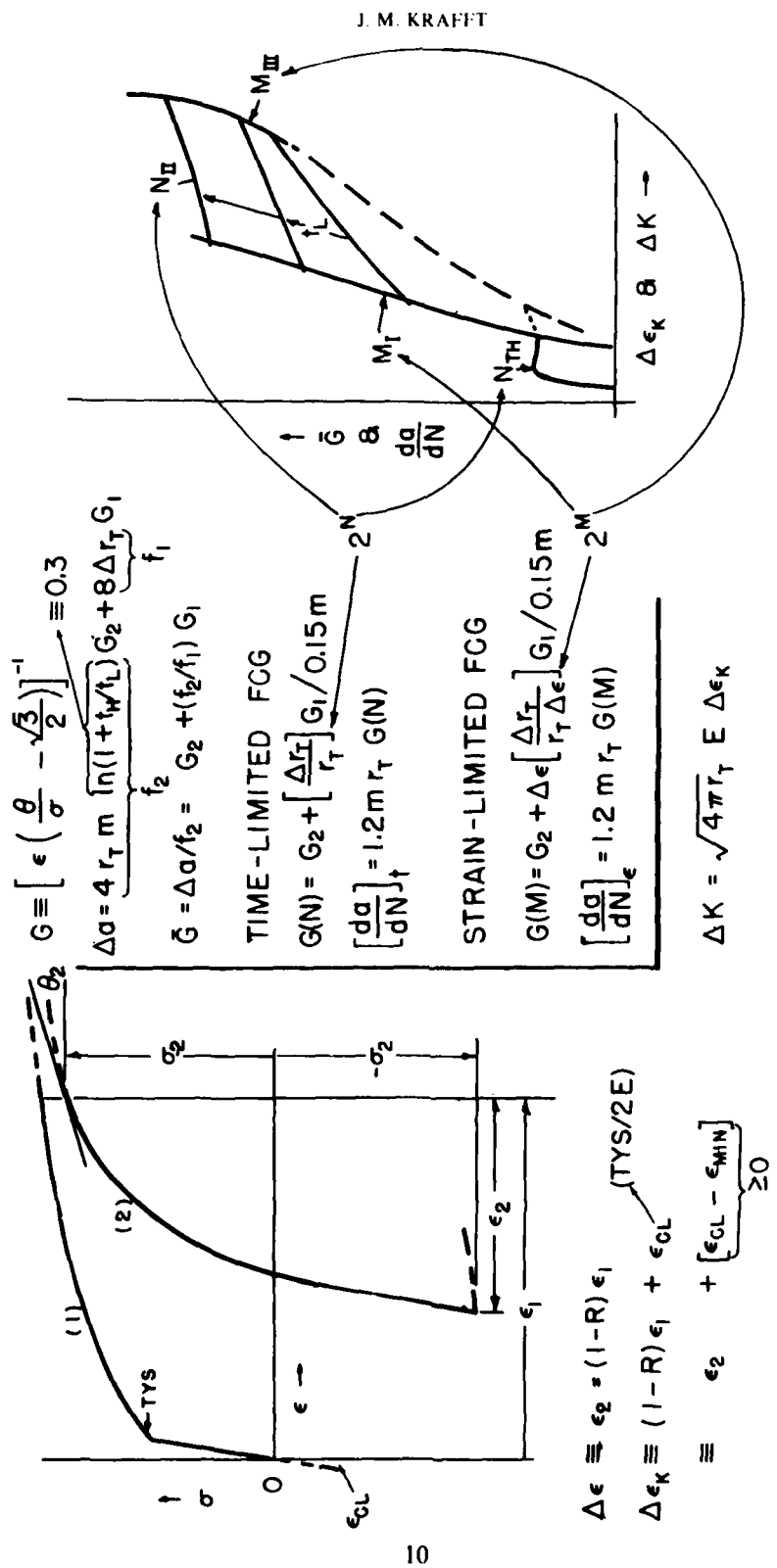


Fig. 1 — Outline of TLM procedure for converting measured shape of monotonic (1) and cyclic (2) stress-strain curves into paths of up to four stages of corrosion fatigue crack growth

making both ordinate and abscissa values functions of the closure strain. Finally, the constant in G_2 was taken as unity rather than $\sqrt{3}/2$. These latter two changes have little effect except that using the K-strains seems to provide slightly more stable G(M) mapping. For this reason they are used in the GRF maps to be shown in this report. However, results and conclusions are scarcely affected by this option. For future work, we intend to use the simpler algorithm as put forth in this section, and so recommend.

One further variation in the plots to be shown is in the calculation of the closure strain. On 300M steels with little tempering, the normal 0.2% offset yield point is markedly higher than the proportional limit. To reflect this, yet not destroy the usual effectiveness of the TYS/2E value, the closure strain was entered as a running variable $\epsilon_{CL} = \sigma_1(\epsilon_1)/\sqrt{3}E$. Again the effect is a minor one, but does improve correlation in a few cases.

3. PREPARING OF GRF PARAMETRIC CURVES

To compare the above-developed algorithm with plotted fatigue crack growth data, it is necessary to construct parametric curve sets of $G(N)$ and $G(M)$ vs $\Delta\epsilon_K$. This task is too laborious for manual calculation and graphing, yet it is readily accomplished with a suitable computer program, large digital computer and plotter. Such a program, available from the Naval Research Laboratory, has been written in BASIC for the NRL DEC PDP-10 computer. The overall procedure involves six steps, summarized in sections to follow.

3.1 Measuring Stress/Strain/Time Curves

The TLIM requires a mechanical stress-strain test of the material of interest. Specimens are preferably excised from used fatigue test specimens, with longitudinal axis normal the fracture plane; ours are 4.32 mm (0.170 in.) diameter, with about 9 mm (0.35 in.) length of uniform cylindrical section between fillets. End buttons 1/2 - 20 NF are threaded in to bottom

firmly in an alignment subpress, then subjected to tensile and compressive deformation in the lower head space of 10 KIP (45 KN) screw-driven Instron machine. It is biased with heavy coil springs to remove backlash in load reversal, in the manner of Coffin and Tavernelli [8].

A four-finger, resistance-strain-gage-instrumented clip gage, Fig. 2, was used to measure longitudinal strain, providing a stress-strain curve. It is designed to fit outside the bi-lobed dimetal strain gage used in previous studies. A cross-plot from the two gages, using the second pen of a two pen X, Y_1, Y_2 recorder, provides instant measure of the Poisson ratio (not shown in this paper). Fig. 3 shows a typical stress-strain curve set.

The Instron was set up to give a constant-load strain rate of about 10^{-3} sec.⁻¹. Data for the stress relaxation exponent m is obtained on the flat region of a cyclic curve by arresting the head and timing, with the highest available amplification, the decay in load. The slope of a log plot of load vs time after arrest is used as the measure of m . Usually two or three replicate tests are performed on a given material, and on each of these several stress relaxation runs.

3.2 Reading and Correcting Flow Data

Values of stress and tangent modulus are scaled directly on the stress-strain curves at selected strain stations. The curve-set to be read is selected from those available after visual comparisons show it to be typical and the record of good quality. Denoting tensile values with subscript T , true values, used in the equations, with none

$$\sigma = \sigma_T (1 + \epsilon_T) \quad (30)$$

$$\theta = \theta_T + \sigma_T (1 + \epsilon_T)(1 + \epsilon_T)^2 \quad (31)$$

$$\sigma = \ln (1 + \epsilon_T) \quad (32)$$

For the cyclic curve, stress is measured from the compressive toe, converted to true stress, then divided by two for the applicable positive portion after centroid zeroing.

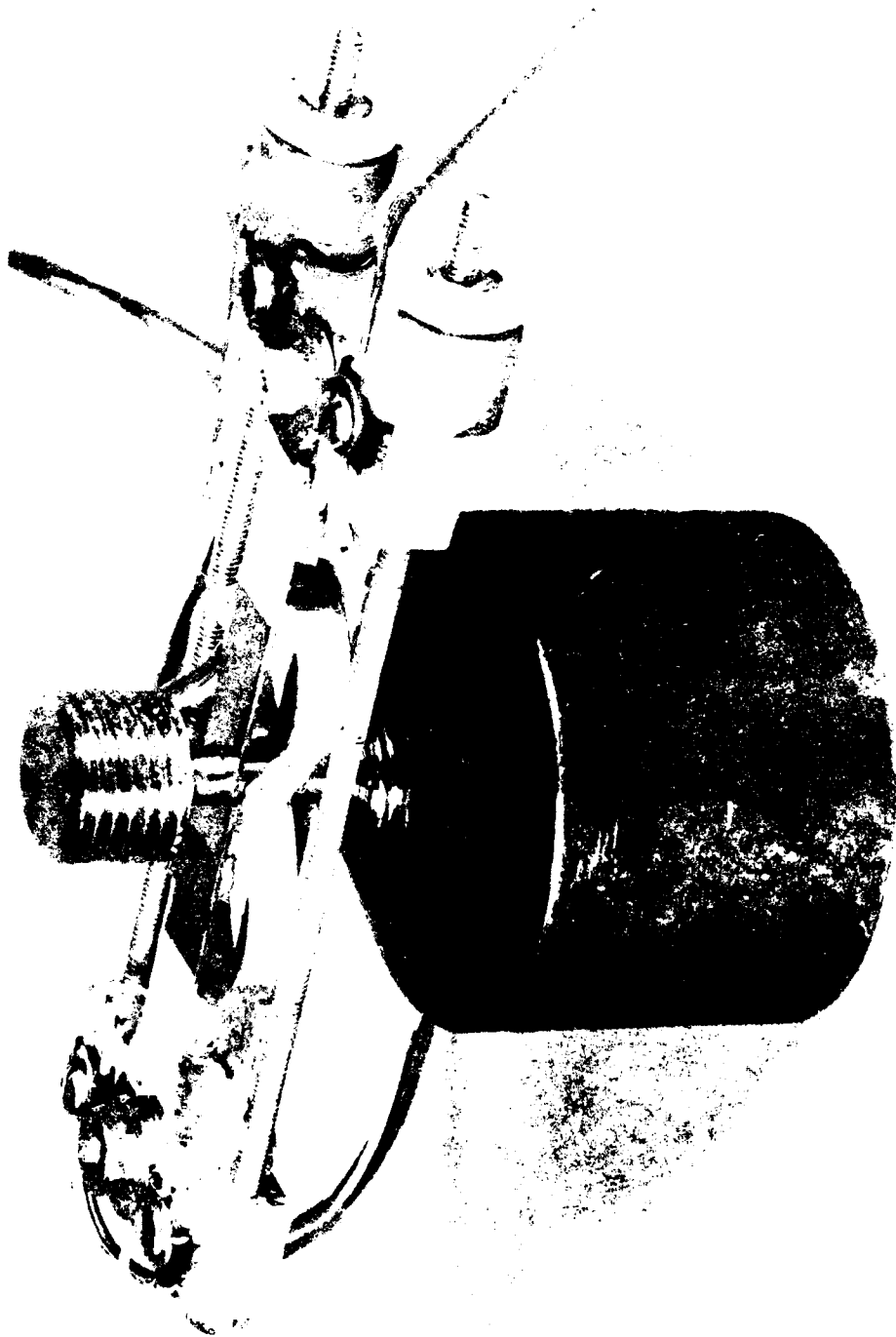


Fig. 1 - Four finger longitudinal strain gage is designed to fit outside of two tubes
to record strain wave velocities inside the aluminum guide cylinder that surrounds

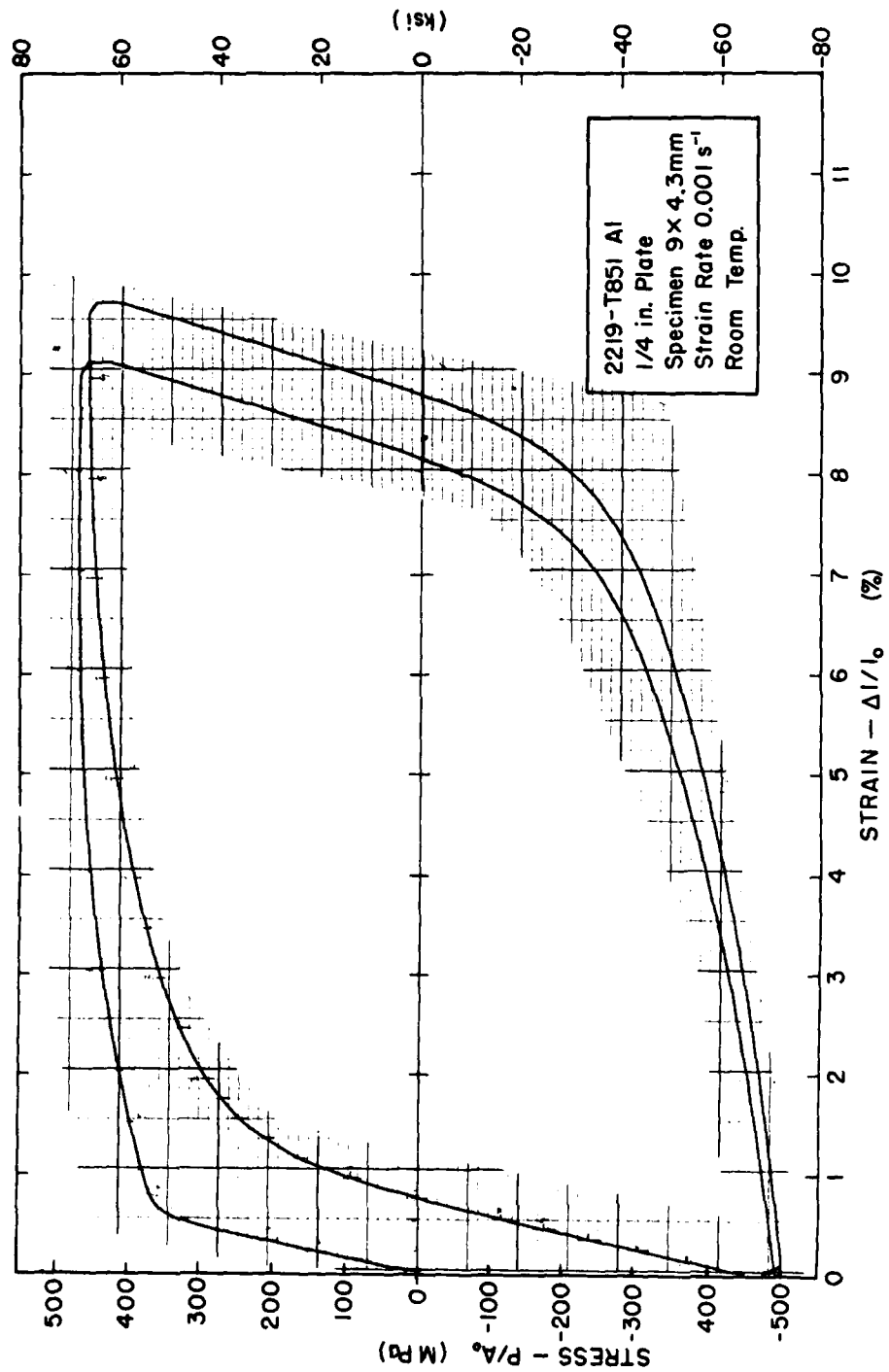


Fig. 3 — Typifying records used in the model; this shows the full monotonic and cyclic stress-strain curves for 2219-T851 Aluminum.

It happens that the strain-limited growth-rate-factor, $G(M)$ of Eq. (23), is extremely sensitive to residual elastic strains; they should be completely removed by use of Eq. (20). To assure this, the measured strain-station value is replaced by one calculated from measured stress σ_2 and cyclic Young's modulus E_2 , and input the computer program as true values. First cycle properties are adequately "trueed" in the program, hence may be input as measured engineering properties.

Monotonic properties of structural steel usually exhibit an upper/lower yield point effect. The ostensibly zero tangent modulus disrupts the model by producing an infinite value of G_1 . On the other hand, good correlations are obtained by removing the yield point effect. Certainly, conditions of crack tip material upon cyclic straining do not allow time to restore the delayed yield effect, as by strain aging processes. The measured yield point effect is removed by fitting a power hardening equation to the region beyond that of the lower yield point, then extrapolating with it back under the measured lower yield plateau. The set of equations used follows:

$$\sigma_1 = \sigma_0 (\epsilon_p / \epsilon_o)^n \quad (33)$$

$$\theta_1 = \left(\frac{\epsilon_o}{n \sigma_o \epsilon_p} + \frac{1}{E_1} \right)^{-1} \quad (34)$$

$$\epsilon_1 = \epsilon_p + \sigma_1 / E_1 \quad (35)$$

The strain hardening exponent n is determined as the slope of a log plot of (measured) σ_1 vs ϵ_1 beyond the lower yield range, and E_1 is the measured monotonic elastic modulus.

Although zero values of measured θ_1 are intractable, the measured stress values produce no infinity. The advantage of using them is that the proportional limit, which along with ϵ_{CL} sets the crack growth threshold level, can be determined from curve measurement. For this paper, values of monotonic σ_1 are used while measured values of θ_1 are used until those of the power law estimate exceed the measured values. This occurs at a strain beyond the proportional limit, so that the threshold strain can be identified with the proportional limit.

J. M. KRAFFT

The monotonic and cyclic flow data is listed in separate data file "programs" in computer storage. The file for a given material is withdrawn and inserted in the calculational program using the BASIC-language WEAVE instruction capability in preparing the program to RUN.

3.3 Pairing Monotonic with Cyclic Properties vs Strain Excursion

Properties from the two curves must be obtained at differing strain levels ϵ_1 and ϵ_2 for given strain excursion $\Delta\epsilon$, Eq. (25). The stations of measurement will rarely correspond. To provide correspondence, a log-uniform set of strain stations is established. In the plots to be shown, a density of 20 stations per decade was employed to approximate the density of measurement points. Greater density, requiring more computing and plotting time, is of little advantage. Using this list, we interrogate lists of cyclic properties vs the strain ϵ_2 to obtain these properties as function of the strain excursion, and at monotonic properties vs the strain of $\epsilon_1(1 - R)$ to obtain these properties as function of the maximum strain. Lists of values are held in memory.

3.4 Pairing Monotonic and Cyclic Properties vs ΔK -strain

The fourth step augments the strain excursion values with the closure strain. But since the augmentation differs for each set, if $R \neq 0$, the new $\Delta\epsilon_K$ strain stations are no longer in registry. Registry is restored by a second round of interpolations, to the same log-uniform strain-station set, now stations in $\Delta\epsilon_K$.

It should be noted that with the algorithm described here, which uses a fixed value of the closure strain and $G_1 = G(\epsilon_1)$ and $G_2 = G(\epsilon_2)$, it is possible to eliminate the second round of interpolations. To do this it is only necessary to convert measured strain values ϵ_1 and ϵ_2 to

$\Delta\epsilon_K$ using Eq. (25-28). However, in earlier algorithms, as indeed in the slight variation on that described above which was used to generate the GRF maps of this report, two rounds of interpolations are required.

3.5 Plotting Growth Rate Factors Maps

The data of step 3.4, or of step 3.3 if only one round of interpolations is used, is then substituted in Eq. (16) for $G(N)$ and (23) for $G(M)$. On the $G(N)$ plot, the range $-21 \leq N \leq -6$ and on the $G(M)$ plot, $-10 \leq M \leq +6$ is found to suffice. The resulting set of values of $G(N)$ vs $\Delta\epsilon_K$ and $G(M)$ vs $\Delta\epsilon_K$ are stored in "PLOT" files in the program, which are called up separately for execution in an HP 7200A Graphic Plotter. The program has provisions for selecting the scale and range of the plot to match the data plot, as well as, optionally, drawing in the coordinate scales, as shown in at least one of each data match illustration to follow. Here both $G(N)$ and $G(M)$ maps have been superimposed to save space. The computer plots of these are more readily distinguished by using contrasting pen colors for each one.

3.6 Installing Matching Guidelines

The matching process involves finding what values of the fitting parameters Δr_T , $\Delta r_T/r_T$ or N , $\Delta r_T/r_T/\Delta\epsilon$ or M provide the best fit of the data. This is done by graphical superposition of *GRF* vs $\Delta\epsilon_K$ maps upon the da/dN vs ΔK data, both of identical (logarithmic) scaling. In doing this, it is convenient to install match guidelines on both the plots. First select an arbitrary point on the crack growth data plot: $da/dN = 10 \mu\text{m}$ cycle; $\Delta K = 10 \text{ MPa} \sqrt{\text{m}}$. Solving Eqs. (14) and (29) using these coordinates, plus an arbitrary value of $d_T = 100 \mu\text{m}$, gives

$$GRF_{REF} = 1/6 \text{ m} \quad (36)$$

$$\Delta\epsilon_{K\ REF} = 1000 (\text{MPa})/\sqrt{2\pi} E_1$$

Other values of d_T can be substituted to establish a line; alternatively one of slope +2 can be

drawn from above-designated reference points, by regarding the 2:1 d_T -sensitivity of GRF vs $\Delta\epsilon_K$. The matching lines shown on the various data-match figures follow this convention. Comparison of G -maps with da/dN data is by superposition of the respective plots with matching lines held coincident. The position of $\Delta\epsilon_{K,REF}$ on the ΔK scale at best match is, conveniently, a value whose square is the size of the d_T process zone in microns.

3.7 Number of Fitting Parameters

Regarding the number of fitting parameters, this model requires from one to five, these of three different kinds. The size parameter d_T is always required. If there is little or no environmental effect, the data should correspond to $G(N) = G_2$ -only, for a one-parameter (d_T -only) fit. If sensitivity to the air environment exists, data will generally correspond to a curve of constant $M = M_{II}$ for a two-parameter fit. In aggressive liquid environments, two additional stages must be characterized: stage I growth by another higher value of $M = M_I$; and stage II bridging I to III with a path of constant $N = N_{II}$ for a four parameter fit. Finally, at high stress ratio, one can detect a "knee" protruding down from the constant $-M_I$ stage I trace which appears to be matched by a curve of very low $N = N_{TH}$ value. The corresponding depth of environmental attack is minuscule, hence not unreasonable. But with it, a maximum total of five fitting parameters are needed. However, the same parameters apply to all positive stress ratios without change.

The two curve-families differ in frequency sensitivity. Curves of constant M , like the stages I and II of CFCG which they track, tend to be frequency-independent, presumably because here the amount of surface attack is limited by the degree of surface distortion, vis a vis plastic deformation of the ligament. On the other hand, the curves of constant N_{II} , as the stage II they track, tend to be frequency/cycle-duration dependent, presumably related to the

time dependency of surface attack or corrosion. One may thus regard growth in stages I and III as of strain-limited surface attack, rather than time-limited, and stage II as of time-limited surface attack, rather than strain-limited.

4. CASE STUDIES

The substantial number of case studies now to be displayed is possible due the generosity of authors who donated specimen material and permission to attempt this modeling. Table I provides a listing of alloy compositions. Table II provides a list of heat treatments and resulting grain size and mechanical properties, and reference to the FCGR data analysis figures of this text. Each of these figures contains the two families of growth rate factor maps, superimposed, from which the fitted curves were selected, and then the FCGR data with selected curves overlaid. The characterizing values of d_T , N_{TH} , M_I , N_{II} and M_{III} , as appropriate, are shown on each figure, but not elsewhere tabulated (except for d_T). However some values of surface attack per

I. Table of Alloy Composition

Alloy	Base +wt%	C	Si	Mn	Ni	Cr	Mo	V	Co	Cu	Al	Nb	S	P
A 36	Fe	0.17	0.29	0.86					0.03				0.021	0.015
BS 4360-50D	Fe	0.17	0.358	1.35	0.07	0.09	0.01		0.17	0.05	0.03	0.023	0.037	
X 65	Fe	0.16	0.33	1.34				0.046				0.031	0.009	0.006
X 70	Fe	0.06	0.28	1.90	0.25		0.39				0.073	0.058	0.009	0.002
SM 58Q	Fe	0.14	0.32	1.30	0.024	0.020	0.023	0.038					0.006	0.022
HT 80	Fe	0.13	0.19	0.94	0.025	0.46	0.14	0.027		0.051			0.007	0.014
HY 130	Fe	0.09	0.26	0.69	5.0	0.48	0.47	0.08		0.05	0.05		0.007	0.009
10 Ni	Fe	0.12	0.07	0.28	10.29	7.03	1.03		8.07				0.006	0.008
4340	Fe	0.40	0.31	0.72	1.85	0.82	0.22						0.020	0.010
300M	Fe	0.42	1.59	0.76	1.76	0.76	0.41	0.10					0.002	0.007
	Base +wt%	Al	V	Me	Fe	C	O	N	H					
R 14A	Ti	6.0	4.1		0.05	0.023	0.06	0.008	0.0050					
R 55A	Ti	6.1	4.0		0.18	0.02	0.11	0.009	0.0069					
R 54A	Ti	6.6	4.4		0.20	0.02	0.18	0.014	0.0058					
R 23C	Ti	6.7	4.3		0.10	0.03	0.20	0.011	0.0060					
W&D 6-4	Ti	6.3	3.9		0.07	0.01	0.14	0.01	0.005					
R 7	Ti	7.4	0.86	1.16	0.14	0.08	0.09	0.004						
R 64A	Ti	7.8	1.1	1.0	0.07	0.03	0.11	0.015	0.0046					
W&D 8-1-I	Ti	7.7	1.0	1.0	0.08	0.022	0.09	0.009	0.005					
	Base +wt%	Cu	Zn	Mg	Si	Mn	Ti	Cr	Fe					
2124	Al	3.9		1.3	0.08	0.54	<0.03		0.14					
2219	Al	6.28	0.025	0.003	0.088	0.25	0.051	<0.0001	0.25					

II. Table of Alloy Heat Treatment, Grain Size, Mechanical Properties

Fig.	Alloy	(cm) Thick	Dir.	(GPa)	(GPa)	(GPa)	ϵ_u	$m^{(2)}$	Grain Size	d_f μm
				E	TYS ⁽¹⁾	UTS ⁽¹⁾	ϵ_u	$m^{(2)}$		
Steel										
4	A36	25	AR	TL	207	0.26/	0.48/	=0.18	0.0072	77
5	BS4360-50D	38	AR	TL	207	0.37/0.37	0.53/0.54	0.26	0.0078	87
6	X65	13	API Spec. SLX	TL	207	0.45/0.46	0.59/0.57	=0.2	0.0064	18
7	X70	19	Control Rolled, API Spec. SLX	LT	207	0.46/0.53	0.63/0.67	0.16	0.0065	45
8	SM 58 Q	12	930° WQ, 650° T, AC	LT	210	0.59/0.59	0.68/0.67	0.09	0.0059	18
9	HT 80	12	880° WQ, 570° T, AC	LT	207	0.74/0.79	0.79/0.82	0.06	0.0052	9.6
10	HY 130	13	830° WQ, 643° T, WQ	LT	207	0.96/	1.09	0.08	0.0054	6.0
11	10 Ni Steel			LT	195	1.32/1.31	1.40/1.35		0.0065	
12	4340/538°	13	843°, OQ, 538° T, AC	TL	—	1.03/	1.08/	0.08	0.0066	9.5
12	4340/427°	13	843°, OQ, 427° T, AC	TL	—	1.25/	1.37/	0.06	0.0059	9.5
12	4340/316°	13	843°, OQ, 316° T, AC	TL	—	1.41/	1.61/	0.05	0.0048	9.5
12	4340/204°	13	843°, OQ, 204° T, AC	TL	—	1.49/	1.88/	0.11	0.0065	2.6
13	310 M/650°	13	870°, OQ, 650° T	208	1.01/1.08	1.17/1.19		0.0057	20 ⁽³⁾	13
14	300 M/470°	13	870°, OQ, 470° T	207	1.28/1.50	1.63/1.68		0.0047	20	6.0
15	300 M/300°	13	870°, OQ, 300° T	207	1.59/1.73	1.97/2.00	0.045	0.0041	20	4.0
16	300 M/100°	13	870°, OQ, 100° T	—	1.07/1.50	2.17/2.34		0.0033	20	1.4
Titanium										
17	R14A	25	1038°/0.5 h, AC, 732°/2 h, AC (BA)	TL	106/115	0.78/0.74	0.87/0.82	0.0118	17	10
18	R55A	25	1038°/0.5 h, AC, 732°/2 h, AC (BA)	TL	120/118	0.83/0.77	0.90/0.87	0.0131	28	12
19	R54A	25	1038°/0.5 h, AC, 732°/2 h, AC (BA)	TL	110/120	0.87/0.82	0.94/0.90	0.065	0.0144	38
20	R23C	25	1038°/0.5 h, AC, 732°/2 h, AC (BA)	TL	106/	0.90/	0.99/	0.07	0.014	11
21	R23C	25	788°/1 h, AC (MA)	TL	117/130	1.01/1.01	1.05/1.04	0.012	5	3.2
22	R23C	25	954°/4 h, HC 760°, HC to 482°, AC (RA)	TL	117/130	0.94/0.93	1.02/1.01	0.10	0.012	9
23	W&D 6-4	16	Mill Anneal	TL	117/116	0.97/0.96	1.01/1.11	0.08	0.0122	7.19
24	R7	6	Mill Anneal	—	117/130	0.97/	1.03/	0.08	0.011	10
25	R64A	25	913°/1 h, AC, 579°/8 h, AC, 538°/2 h, AC	TL	130/136	1.00/0.96	1.08/1.03	0.11	0.0118	9
26	R64A	25	1093°/1 h, AC	TL	126/128	0.84/0.79	0.97/0.90	0.10	0.0117	60
27	W&D 8-1-1	16	Duplex Anneal	TL	121/122	0.88/0.84	1.05/1.04	>0.12	0.0098	14/14 ⁽⁴⁾
Aluminum										
28	2124	51	AR	LT	71/	0.46/0.46	0.51/0.50	0.055	0.007	6.5
29	2219	76	AP	LT	68/	0.37/0.36	0.48/0.46	0.01		6.4

Heat Treatment Abbreviations Temp in °C

AR = As Received, Normal He. Treatment Presumed.
 WQ = Water Quench.
 OQ = Oil Quench.
 T = Temper.
 AC = Air Cool.
 FC = Furnace Cool.
 HC = He purge Cool to effect AC rate

(1) Meas/Author's values shown

(2) Room Temperature value of m

(3) Prior Austenite Grain Size

(4) From 1st Cyclic Excursion Curve

cycle, as calculated from the figures, are plotted in summary figures. The figure captions contain reference to the author of the FCGR data, and/or to the donor of specimen material. The figures are ordered in the grouping and sequence of Table II. Some notes on particular cases of the data collection follow.

4.1. Iron Based Alloys

Figures 4 to 16 display TLIM analysis of the sixteen steels of differing composition and/or heat treatment.

Linear elastic fracture mechanics parameters can be applied to mild steels because fatigue crack growth occurs at ΔK levels well below K_{Ic} . Actually the fatigue instability limit, K_{fc} , the ΔK for indefinitely rapid FCG rate, is generally much less than K_{Ic} . In the TLIM, this is associated with cyclic hardening, which reduces, by as much as a factor of 2 to 3, the cyclic strain for maximum (tensile) load. Thus even in a steel as soft as A-36, Fig. 4, a substantial part of the growth curve can be measured, and fitted by TLIM procedures. However at a stress ratio as high as 0.8, only the threshold region can be interpreted with K-parameters. Here the general shape of the threshold plateau does appear to be roughly followed by the $N_{TH} = -18$ curve. A more refined closure strain algorithm is needed for more accurate prediction in this region. The manner of removing upper yield point effects is a factor here.

The TLIM match of BS4360 Grade 50D in both room air and 5-10 degrees Centigrade sea water, Fig. 5, seems rather satisfactory, as also that for line pipe steels X65 and X70 in air and room temperature salt water, Figs 6 and 7. In X65, Fig. 6, the shift to the right with frequency of the low H_2S crude data could be an effect of strain rate on the size and shape of the stress-strain curve, to be discussed later.

J. M. KRAFT

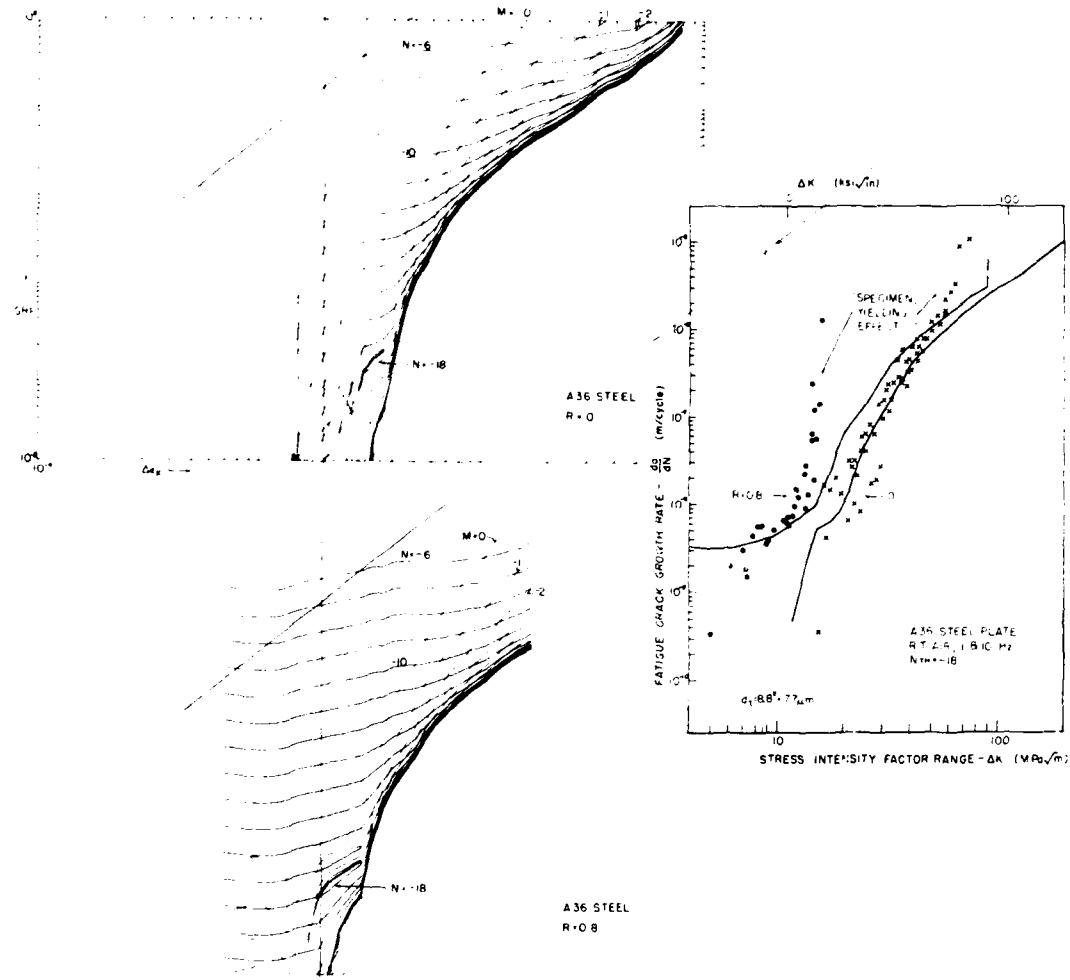


Fig. 4 — Growth-rate-factor parametric curves matched to Stonesifer FCGR data on A-36 steel, Ref. 9.

NRL MEMORANDUM REPORT 4161

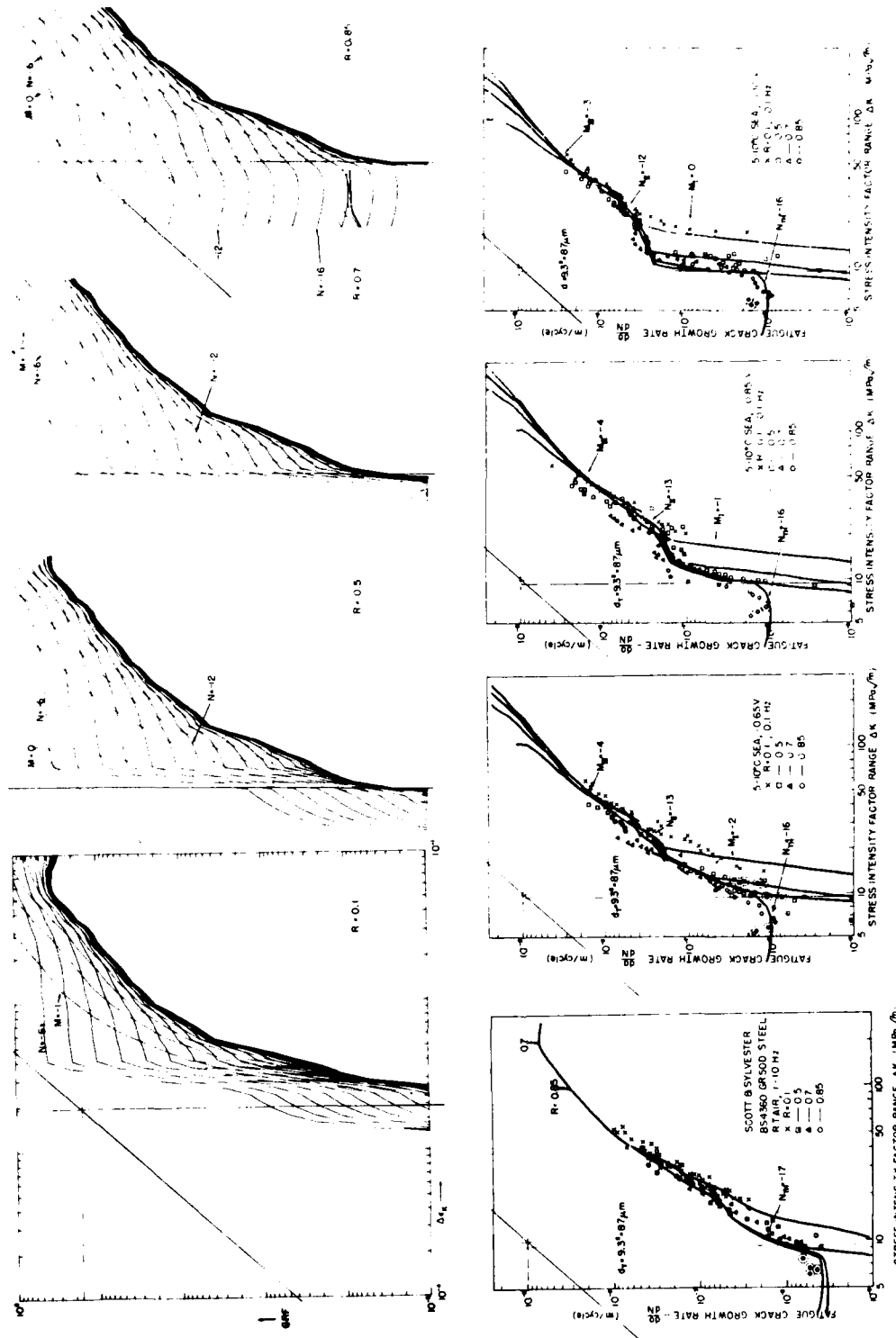


Fig. 5 — GRF curves for BS4360 Grade 50D steel matched to GFGGR data of Scott and Sylvester. Ref. 10. The curves shown are from stress strain data at 25°C; another set from 7°C, was used for the air environment test. Authors' designation experimental artifact by enlarged circles around data points lower left block.

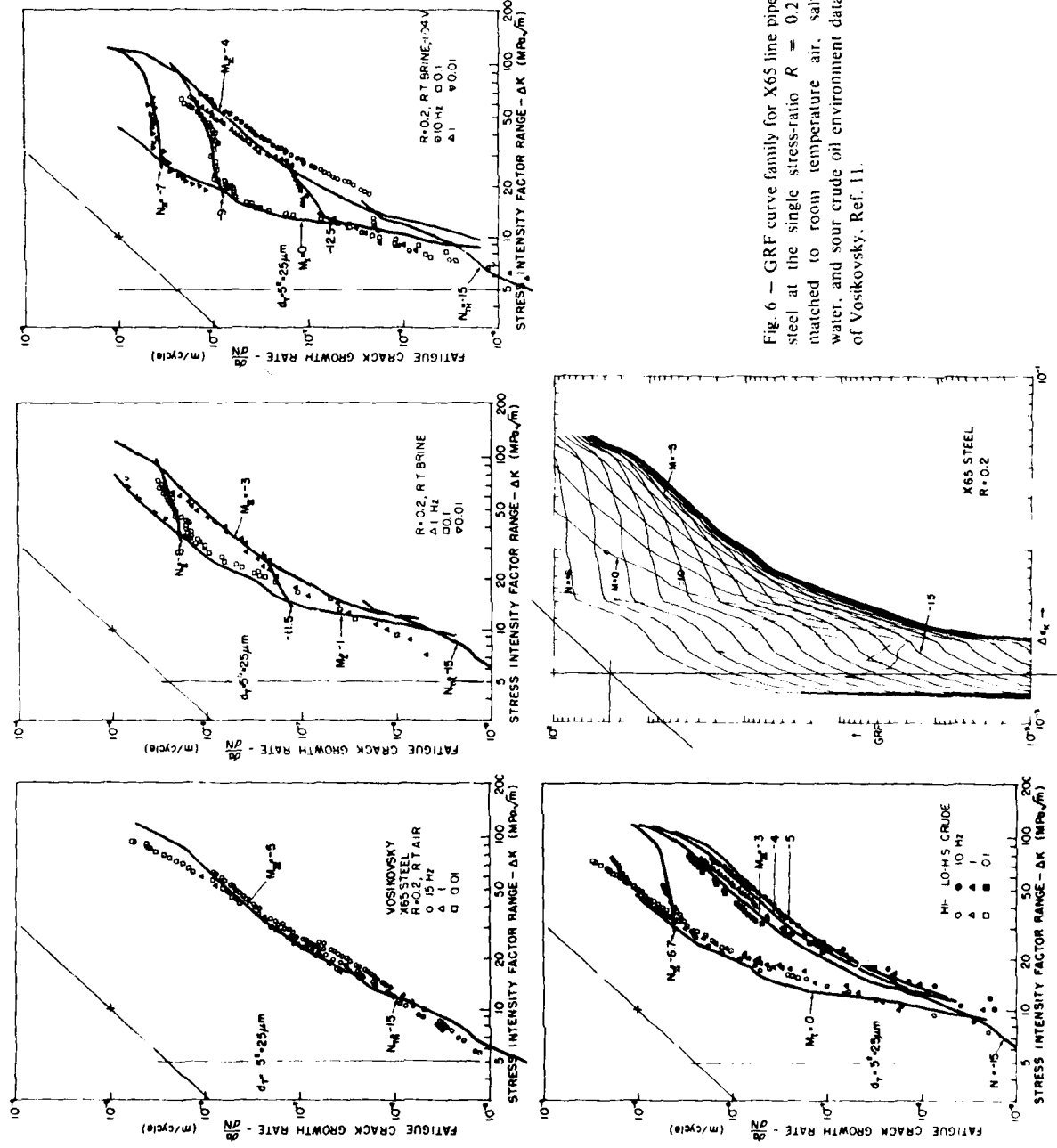


Fig. 6 — GRF curve family for X65 line pipe steel at the single stress-ratio $R = 0.2$, matched to room temperature air, salt water, and sour crude oil environment data of Vosikovsky, Ref. 11.

NRL MEMORANDUM REPORT 4161

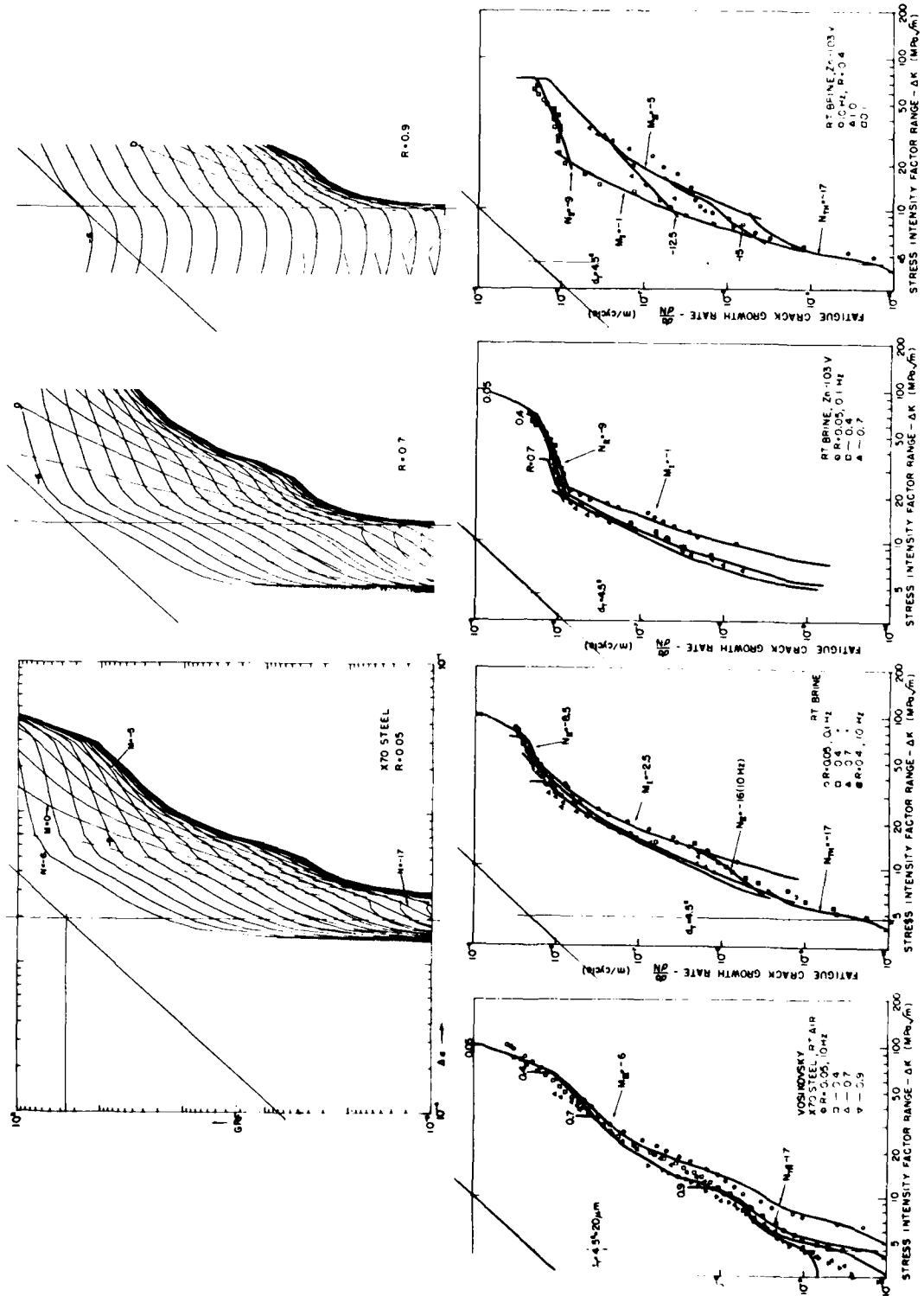
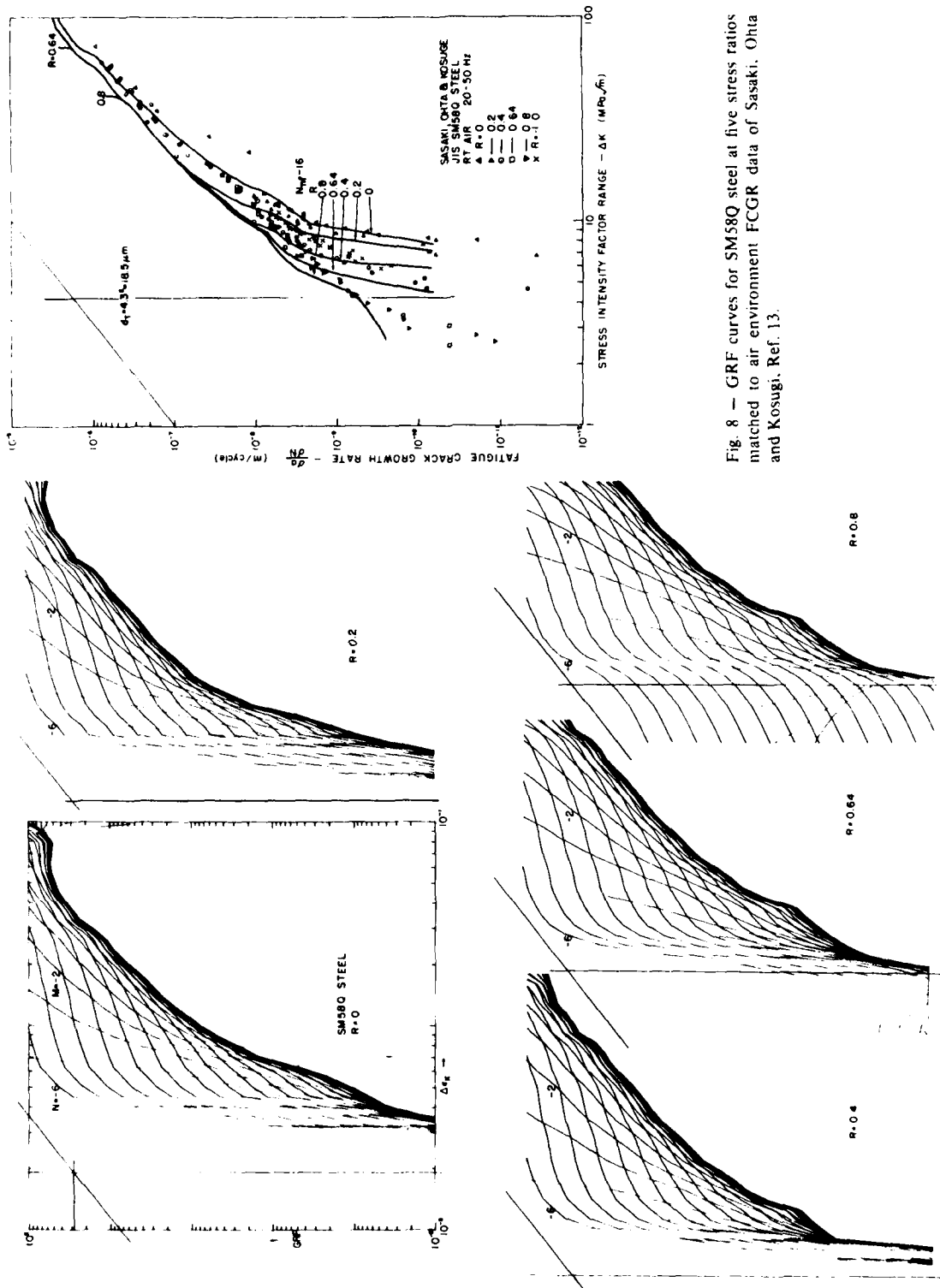


Fig. 7 - Growth-rate-factor curves for X70 line pipe steel at three stress ratios matched to air and salt water environments [CGR data of Vankovsky, Ref. 12]

J. M. KRAFFT



NRL MEMORANDUM REPORT 4161

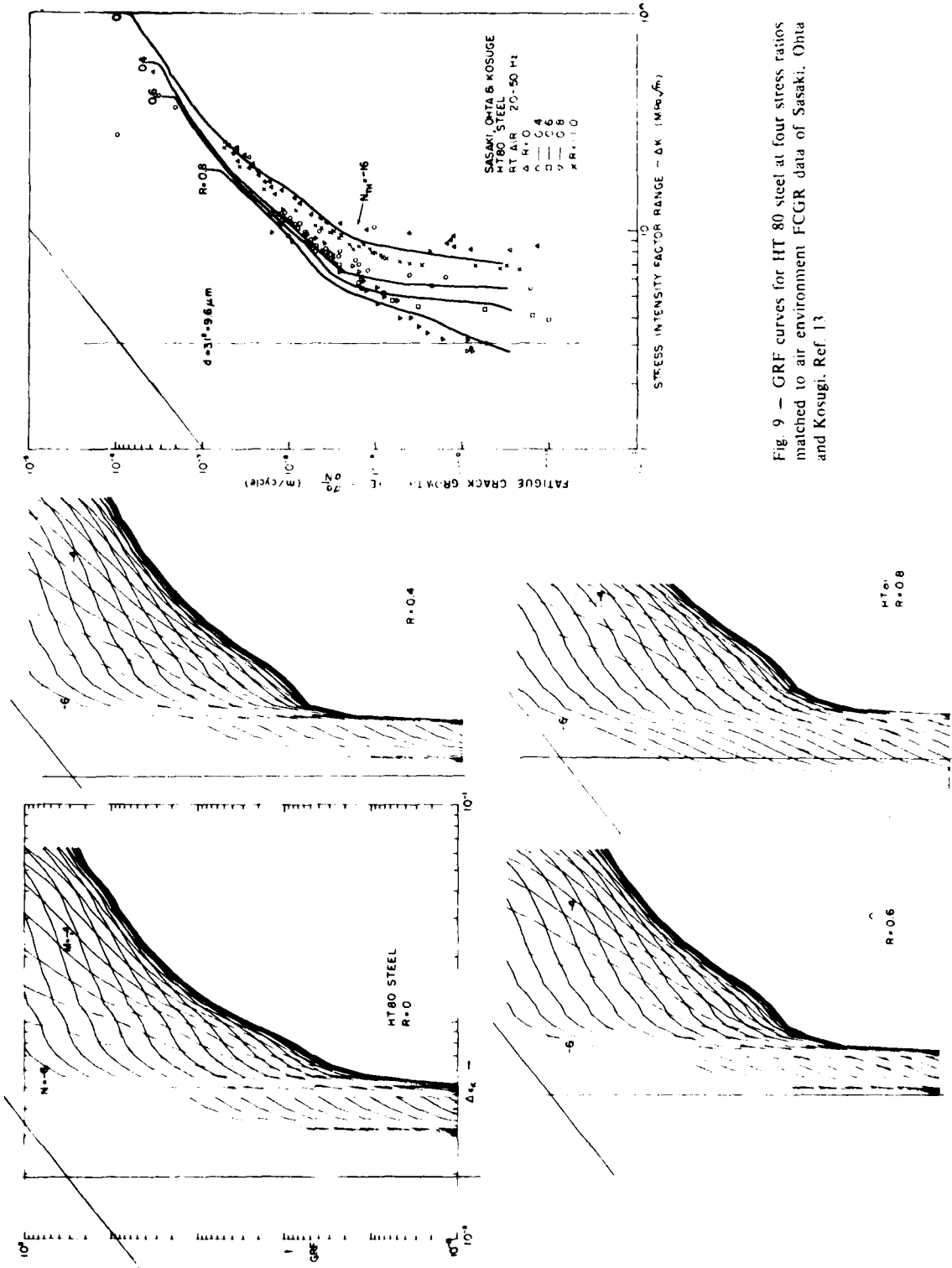


Fig. 9 - GRF curves for HT 80 steel at four stress ratios matched to air environment FCGR data of Sasaki, Ohta and Kosugi, Ref. 13.

J. M. KRAFFT

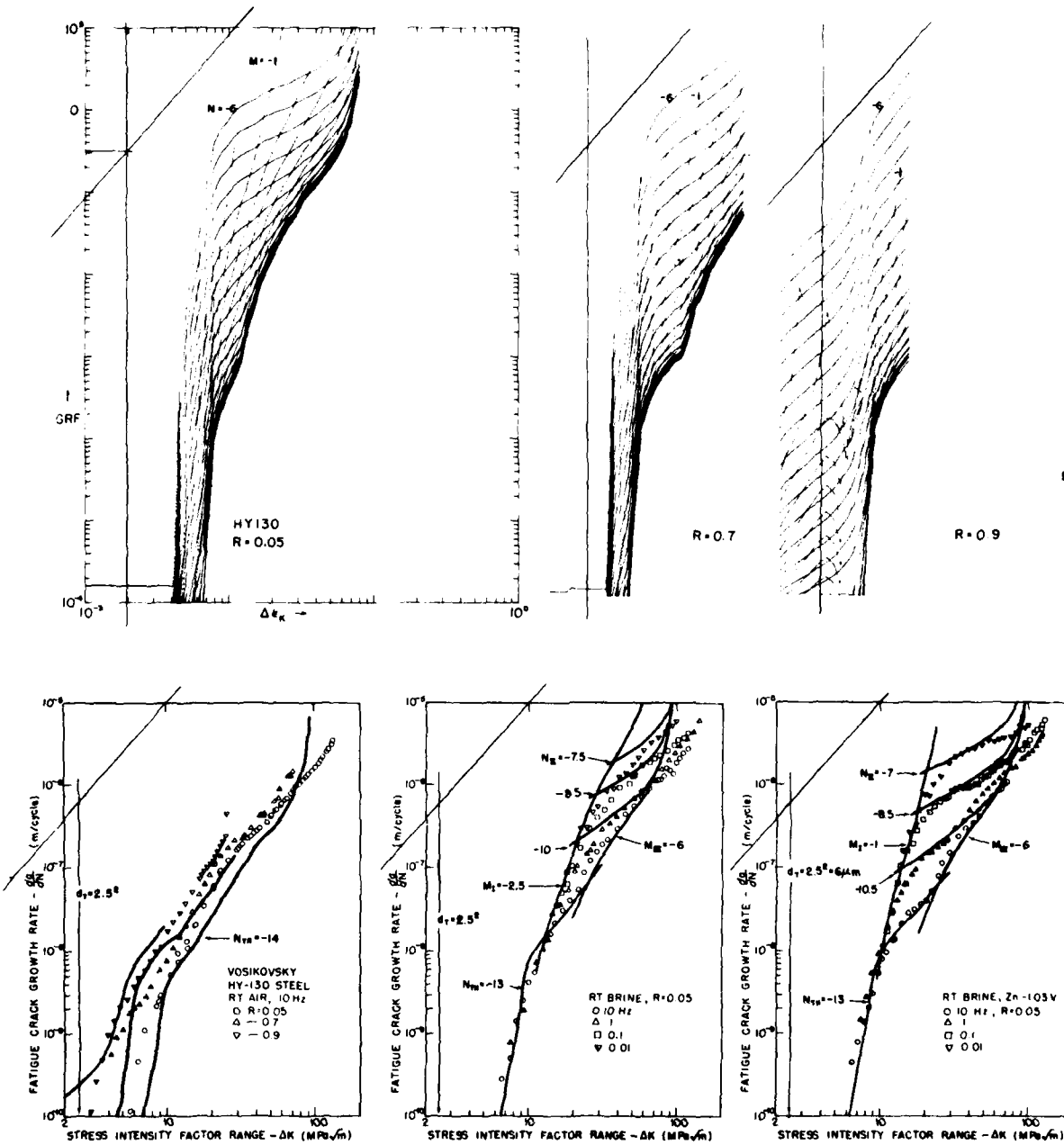


Fig. 10 — Growth-rate-factor curves for HY 130 steel at three stress ratios matched to air and salt water environment data of Vosikovsky, Ref. 14

NRL MEMORANDUM REPORT 4161

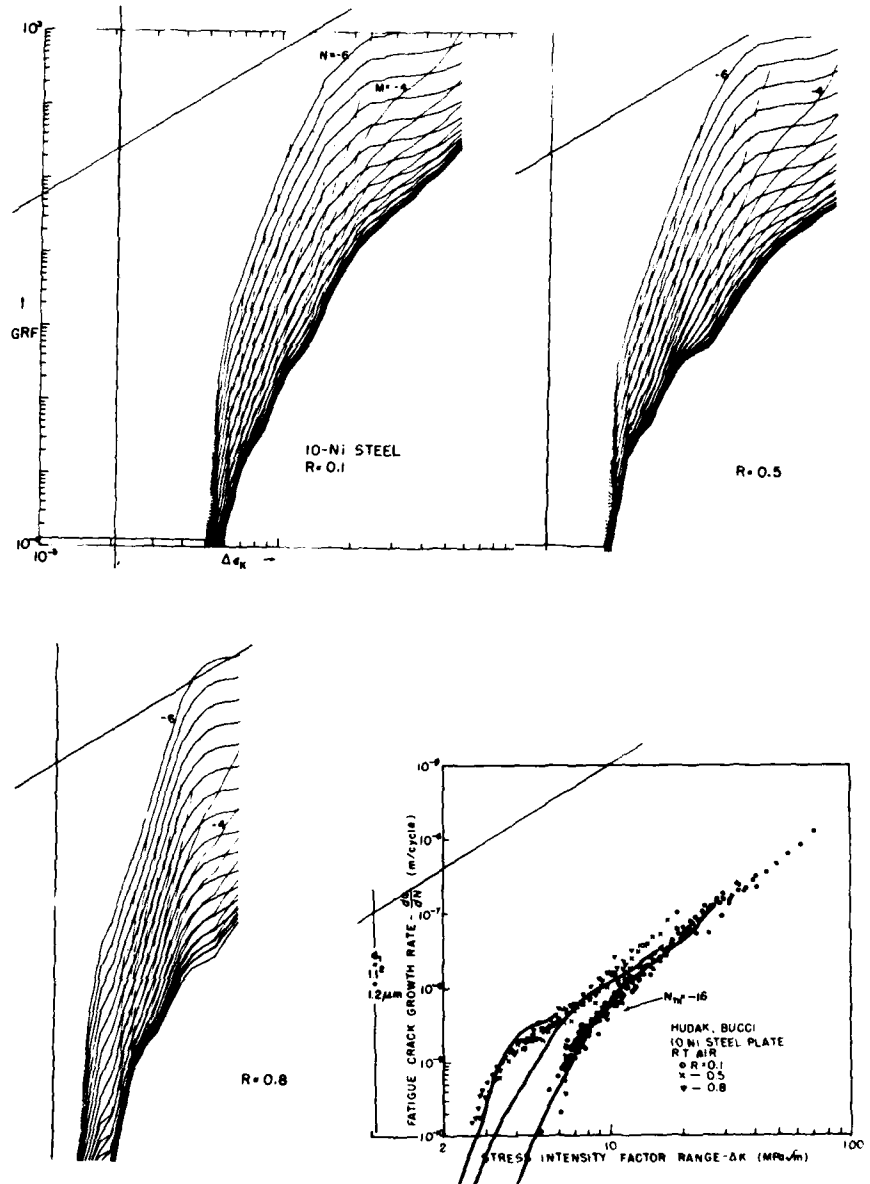


Fig. 11 — GRF curves for 10-nickel steel at three stress ratios matched to air FCGR data of Hudak and Bucci, Ref. 15.

J. M. KRAFFT

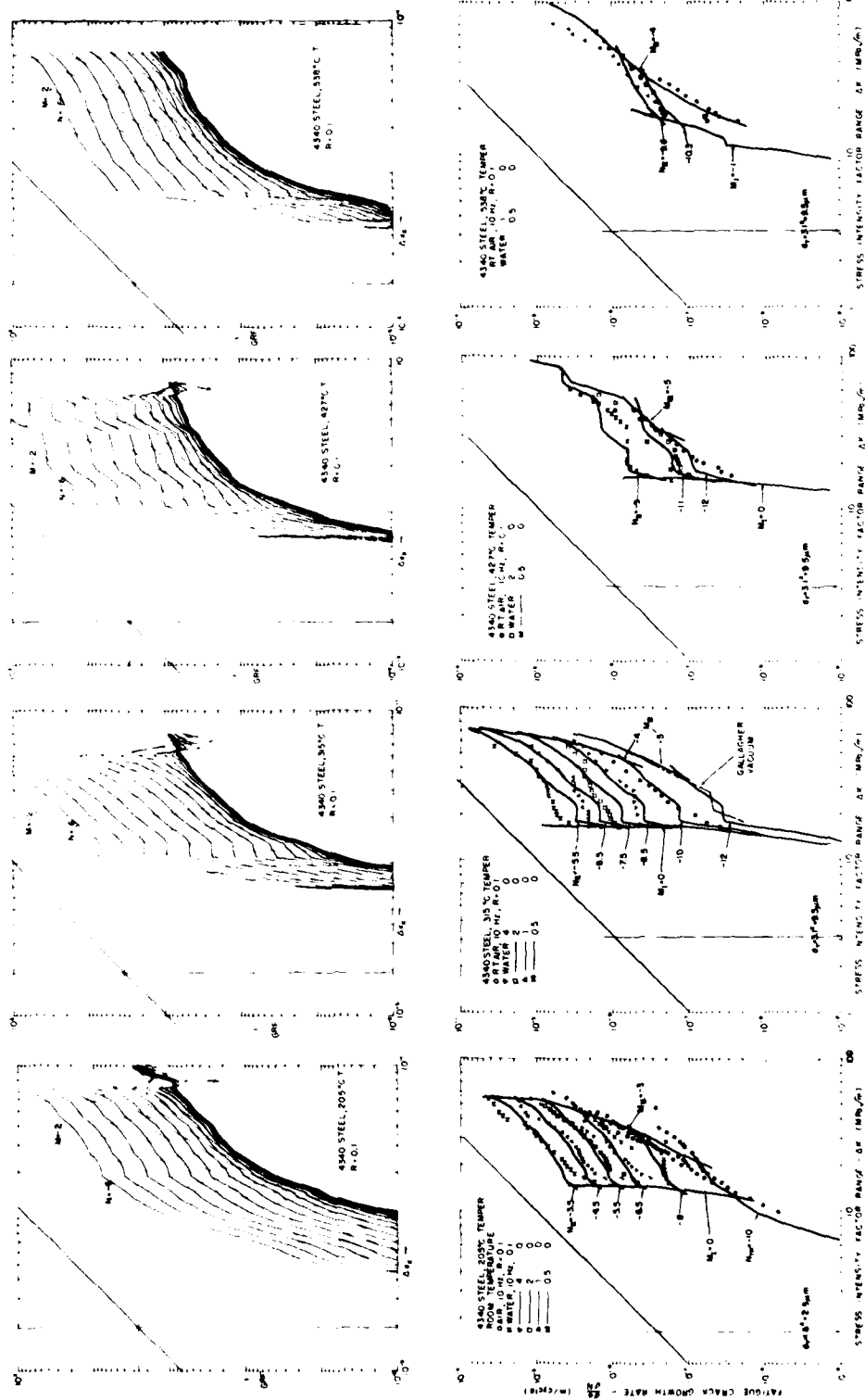


Fig. 12 — GRF curves for each of four tempts of 4340 steel matched to CFCGR data in air and fresh water environments by Stoner, reported in Ref. 3

NRL MEMORANDUM REPORT 4161

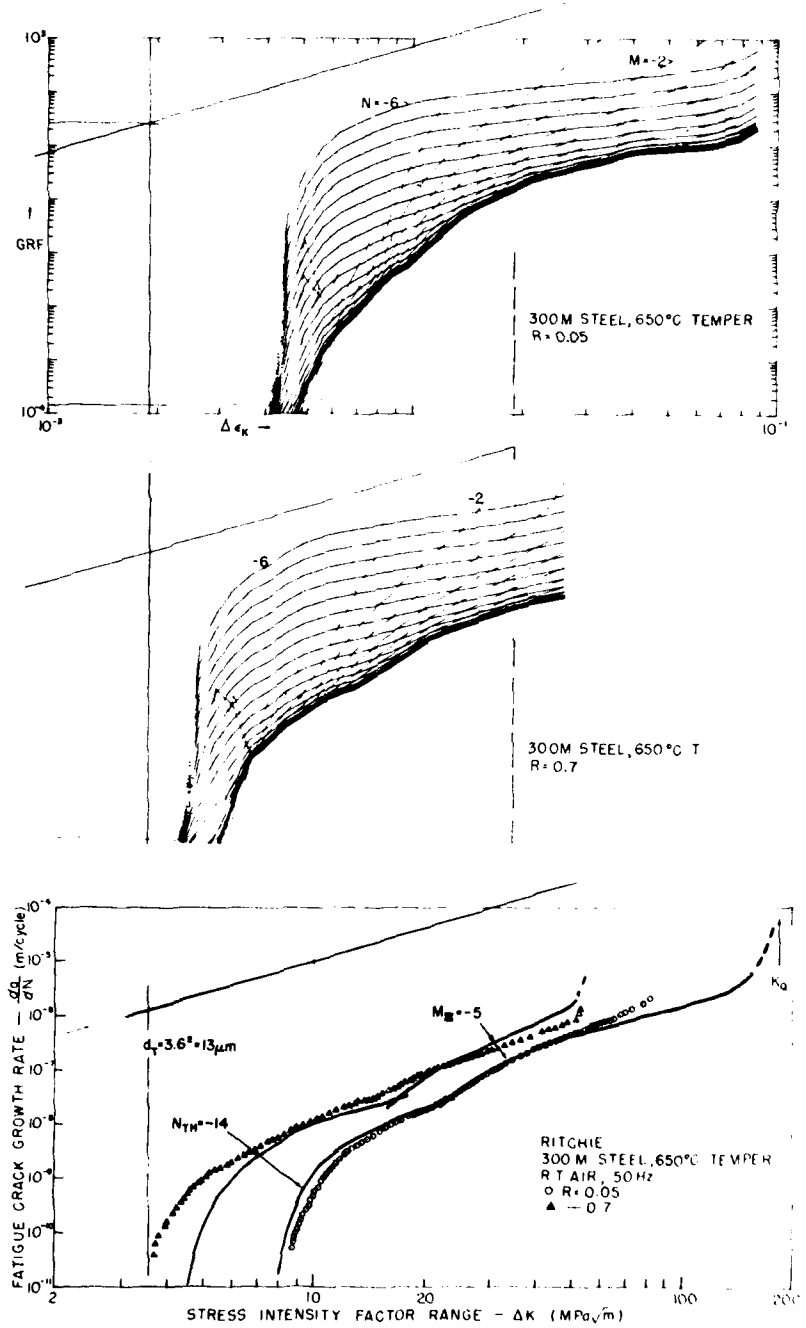


Fig. 13 — Growth-rate-factor curves for 300M steel tempered at 650 degrees Centigrade at $R = 0.05$ and 0.7 matched to air environment data of Ritchie, Ref. 16.

J. M. KRAFT

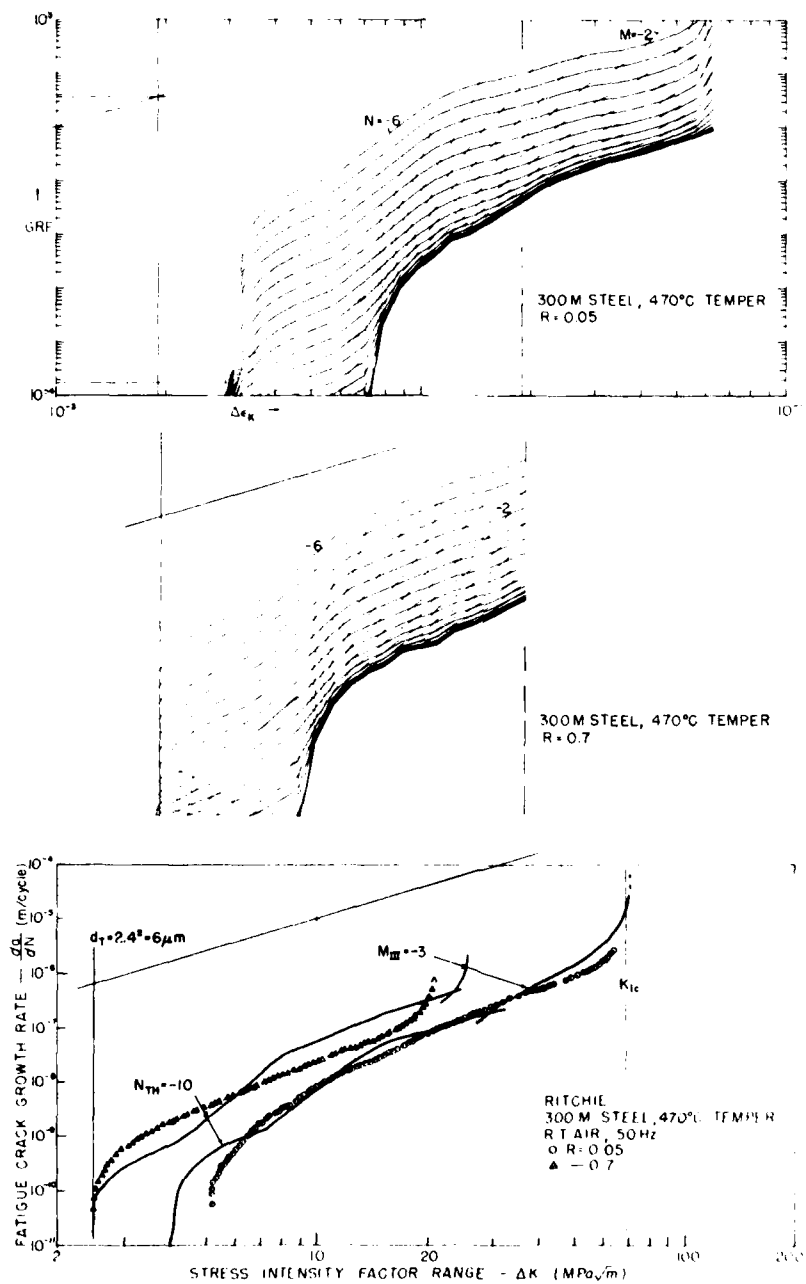


Fig. 14 — Growth-rate-factor curves for 300M steel tempered at 470 degrees Centigrade at $R = 0.05$ and 0.7 matched to air environment data of Ritchie, Ref. 16

NRL MEMORANDUM REPORT 4161

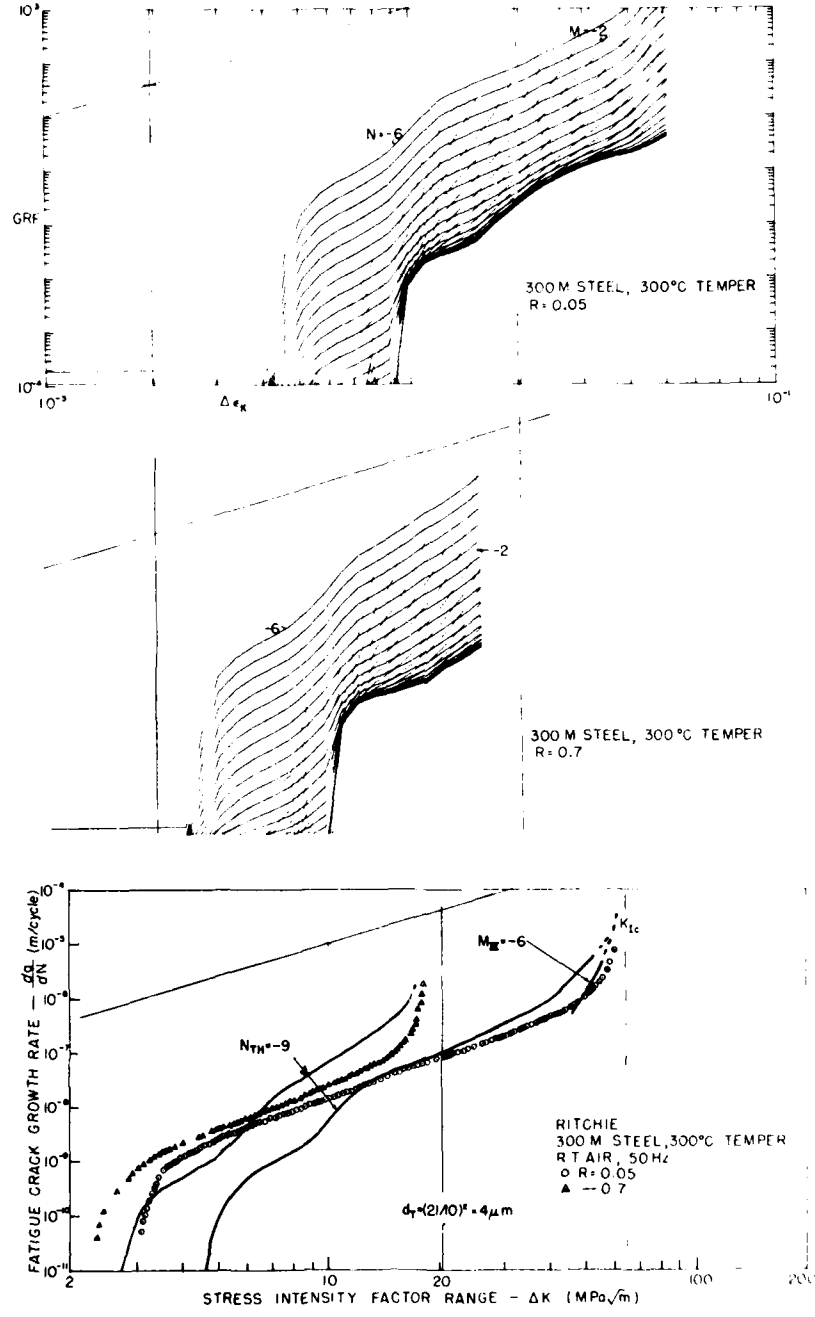


Fig. 15 — Growth-rate-factor curves for 300M steel tempered at 300 degrees Centigrade at $R = 0.05$ and 0.7 matched to air environment data of Ritchie, Ref. 16.

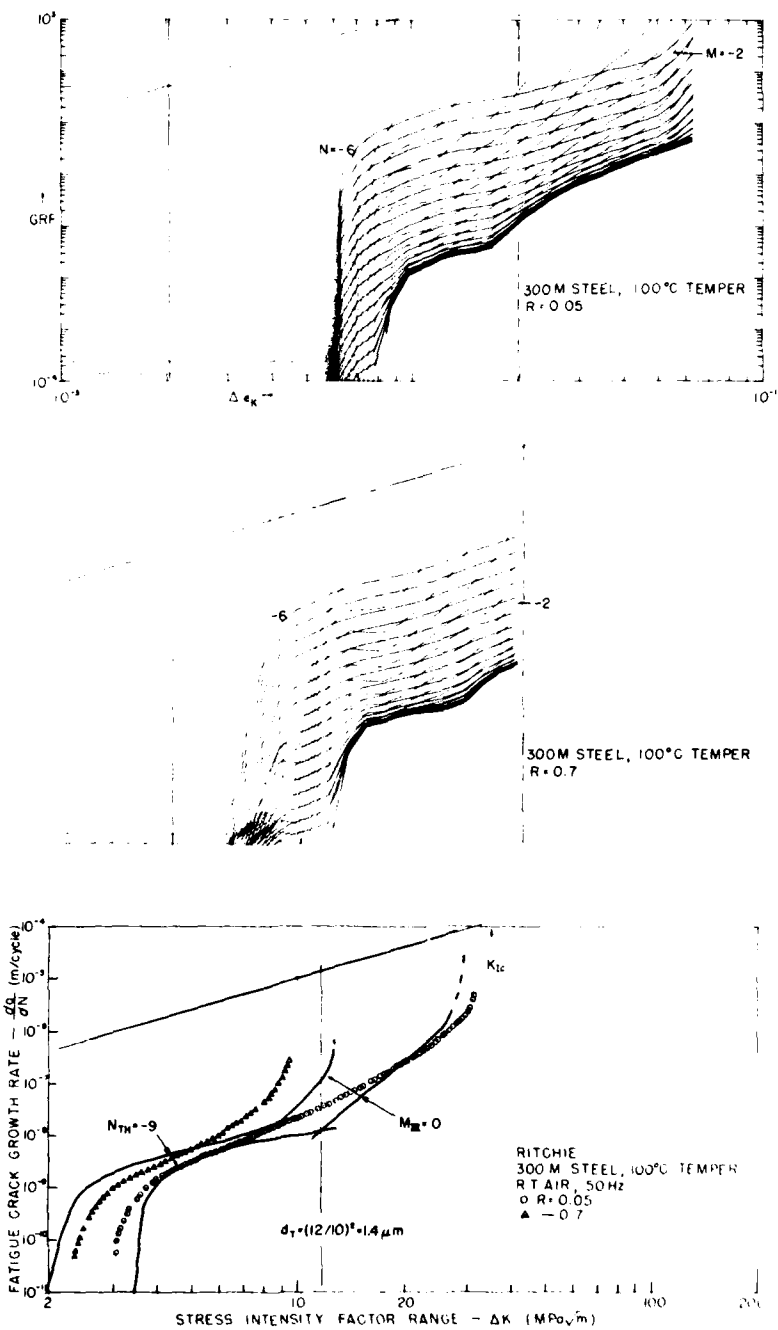


Fig. 16 — Growth-rate-factor curves for 300M steel tempered at 100 degrees Centigrade at $R = 0.05$ and 0.7 matched to air environment data of Ritchie, Ref. 16.

The extensive R-effect data in air on SM58Q and HT80 steels, Figs. 8 and 9 is reasonably well matched. The TLIM curves for $R = 0$ does separate from the high-R curves, in mid-range ΔK , more than the data, particularly in the SM58Q. Here the modification of the TLIM equations to include the closure strain in the gradient strain term of G_1 and G_2 tends to exaggerate this discrepancy.

Regarding HY130 and the 10 Ni steel, Figs. 10 and 11, there is some difficulty in matching both ends of the crack growth range with the growth rate factor maps. If one fits to favor the threshold region, as has been done here, the run-out in the fatigue instability region falls short; and vice versa. The behavior is much as though the closure strain term is too large. It is possible that residual stress from the quenching operation in heat treatment could have an effect. Significant influences of this kind have been reported by Sullivan and Crooker [29] and by Ritchie, Smith and Knott [30]. Another problem is that the monotonic tensile stress-strain curves of these materials is so extraordinarily flat that it is difficult to determine the point of maximum load. Large effects of strain rate, via cyclic frequencies, are likely here. In view of these uncertainties, present matching parameter values on these two steels should be regarded as provisional.

If residual stress is a factor in the high strength quenched and tempered steels, what about 4340 and 300M? In the 4340, Fig. 12, the data is not critical as the growth threshold region has not been characterized, hence the model is easily fitted to mid and upper ranges. In the 300 M a full range of FCG data is available. Indeed the higher tempering temperatures, hence lower residual stress, give the better fits, particularly in the threshold region. A point of caution here is that the tensile specimens of 300M were heat treated separately on plate material provided by Ritchie; they were not cut out of heat treated fracture specimens, as is our preferred practice. It appears that this has failed to develop the strength properties of the test specimens, as seen in Table II, where the two values are compared.

4.2. Titanium Based Alloys

Figures 17 to 27 display TLIM analysis of the seven Ti-6Al-4V alloys and four Ti-8Al-1Mo-IV alloys of differing composition and/or heat treatment.

The Yoder data on Ti-6-4, as on Ti-8-1-1, was meant to characterize changes in FCGR as a function of microstructural and interstitial concentration changes. Hence the amount of data collected, though carefully measured, was only as extensive as required to characterize the mid-range growth rates. This includes the mid-range slope inflection, which Yoder associates with correspondence of grain size and the reverse plastic zone size. With this, the TLIM curve fit is not as rigorously bounded as with more extensive data sets. However the curve matching seems fairly tight, and some sort of inflection point is suggested directly from the shape of the constant- M_{II} curves.

The two data collections from Wanhill and Döker, Figs. 23 and 27, touch on the question of two stage hardening effects. With continued cycling, the strain hardening rate of many titanium alloys tends to decrease, then at about half of the strain excursion, increase to recover the earlier strength loss. It was thought that the abrupt jump in growth rate shown by these authors might be associated with this effect. To this end, the second full cyclic excursion, showing a moderate but not fully developed two stage hardening, was measured. The second cycle map does appear to provide a closer fit of the FCGR data. However, first cyclic curves also fit reasonably well and since these had been used in all other cases, the d_T value from its match is used in comparisons of fitting parameters to follow. This is only a token "glimpse" of the subject; much more should be done on it.

NRL MEMORANDUM REPORT 4161

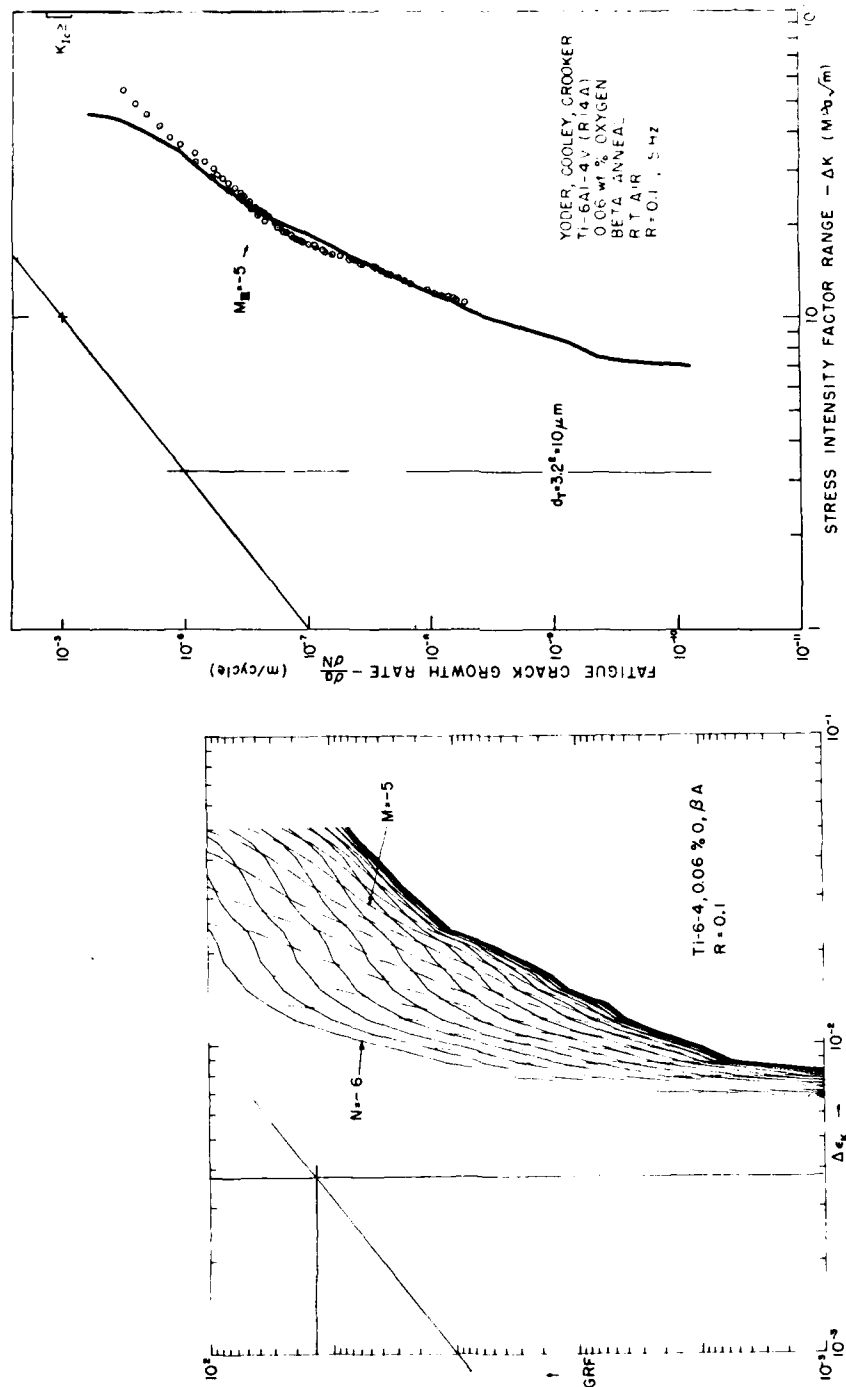


Fig. 17 — Growth-rate-factor curves for Ti-6Al-4V, 0.06% oxygen, beta anneal, matched to air FCGR data of Yoder, Cooley, and Crooker, Ref. 17.

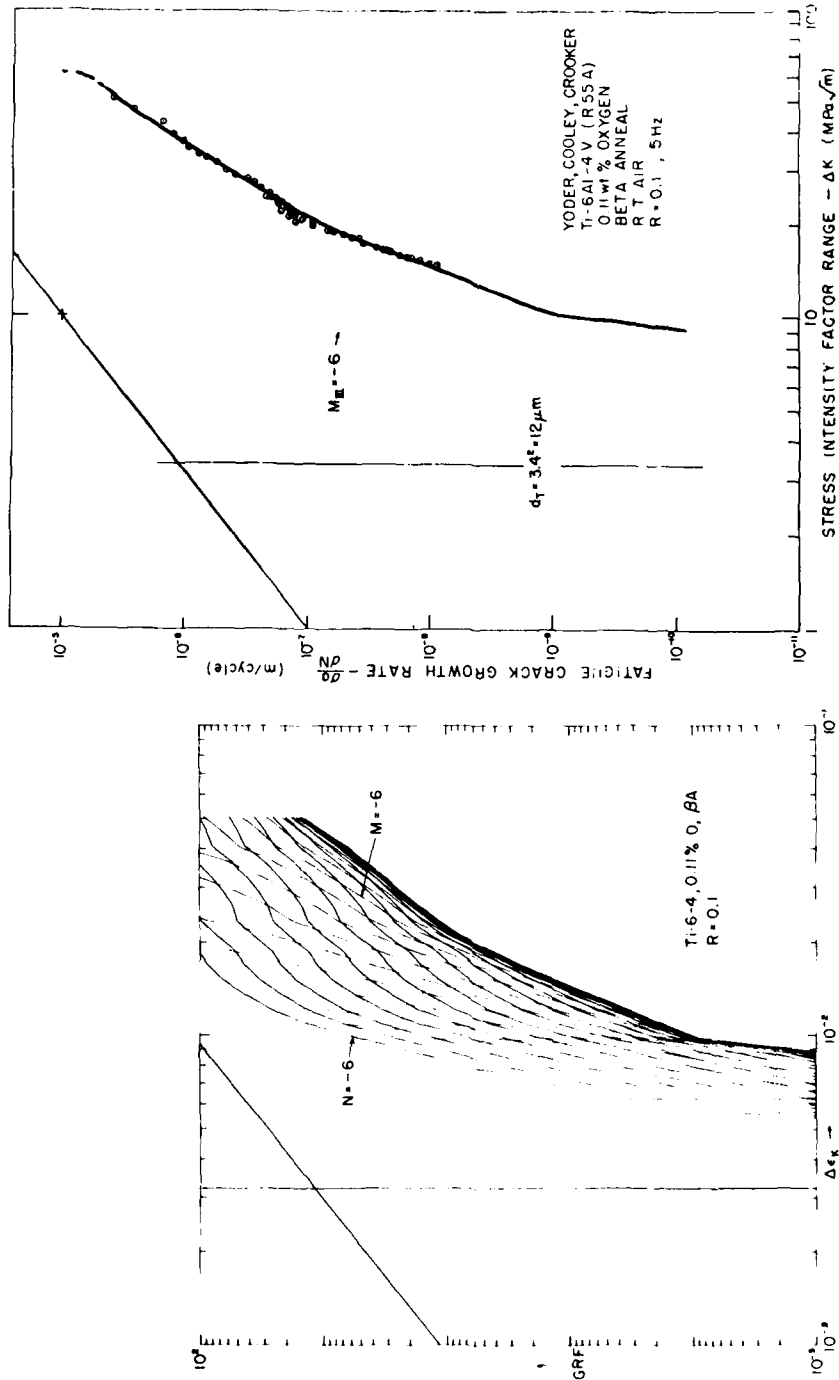


Fig. 18 — Growth-rate-factor curves for Ti-6Al-4V, 0.11% oxygen, beta anneal, matched to air FCGR data of Yoder, Cooley, and Crooker, Ref. 17.

NRL MEMORANDUM REPORT 4161

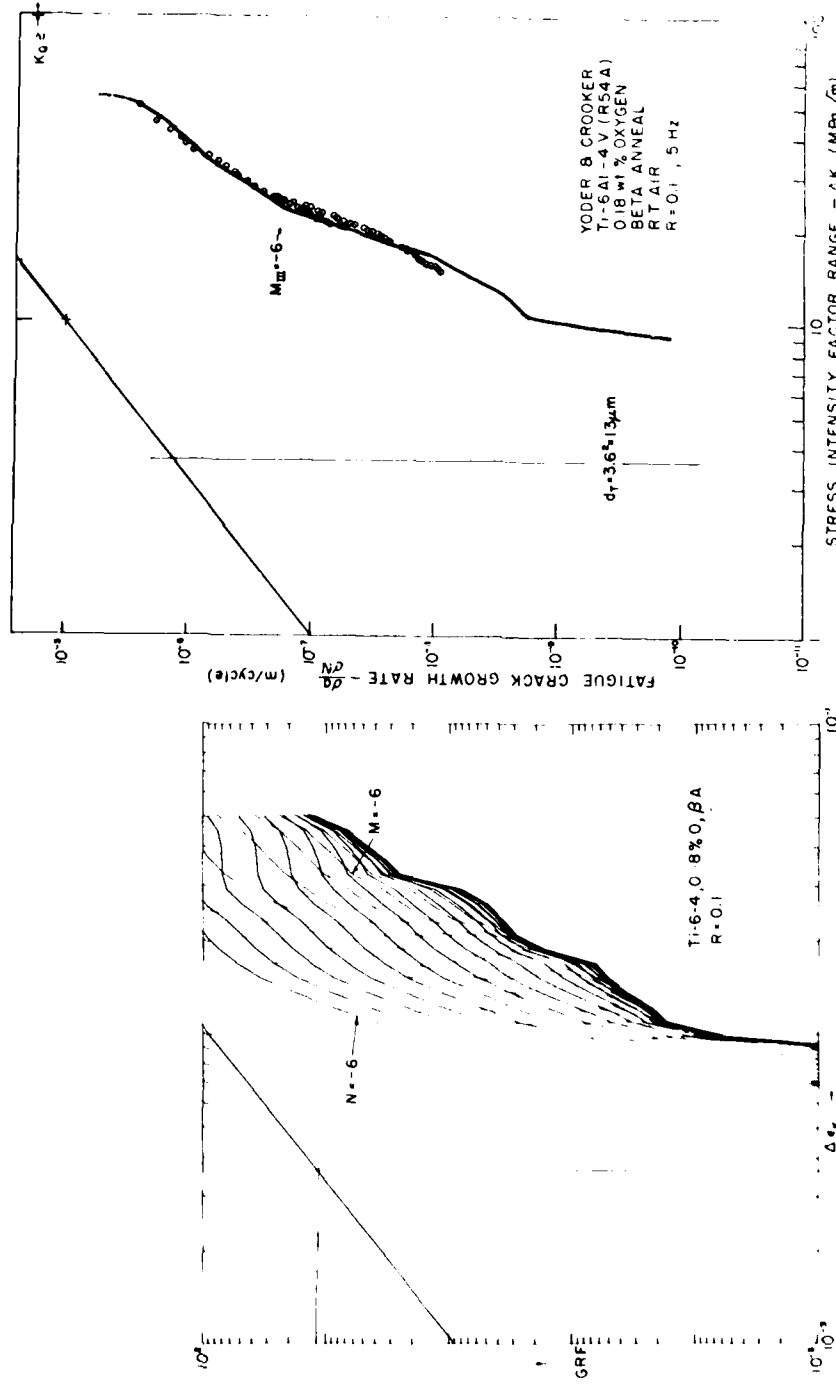


Fig. 19 - Growth-rate-factor curves for Ti-6Al-4V, O_2/N_2 oxygen, beta anneal, matched to air FCC GR data of Yoder, Cooley, and Crooker. Ref. 17

J. M. KRAFT

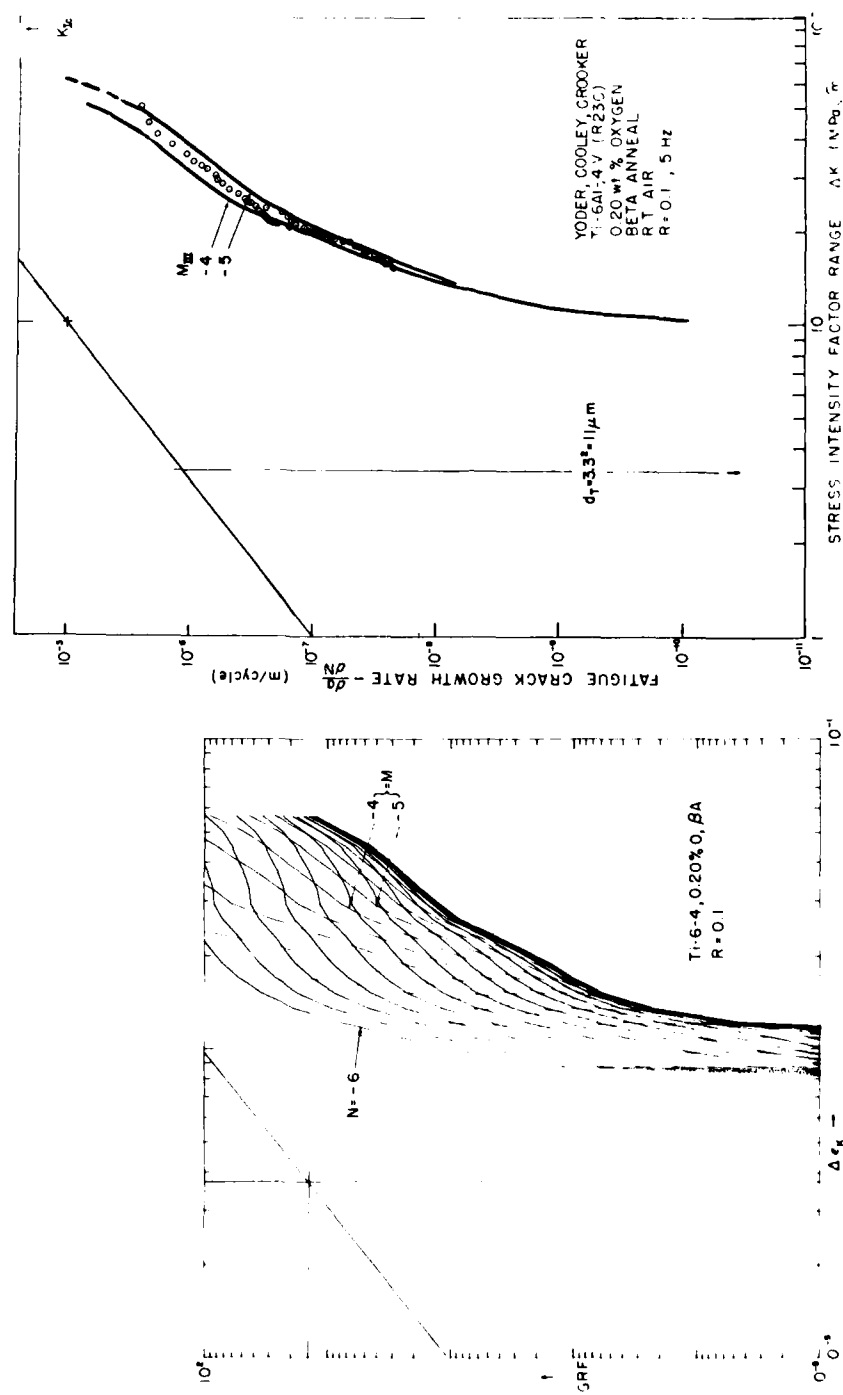


Fig. 20 — Growth-rate-factor curves for Ti-6Al-4V at 20% oxygen, beta anneal, matched to air FCGR data of Yoder, Cooley, and Crooker. Ref. 17.

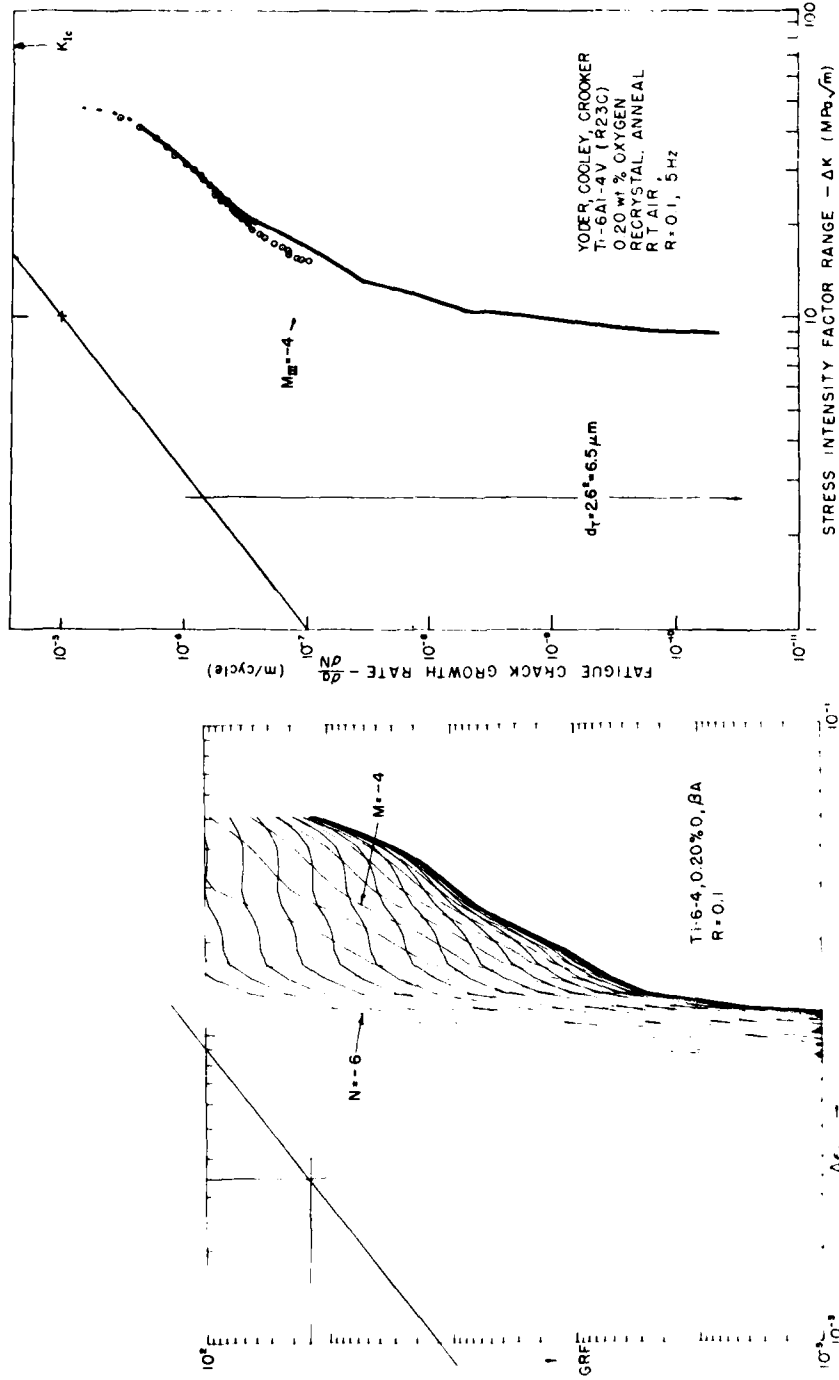


Fig. 21 — Growth-rate-factor curves for Ti-6Al-4V, $\sigma^{(2)} = 290$ mpsi, oxygen, recrystallization anneal, matched to air FCGR data of Yoder, Cooley, and Crooker, Ref. 18 and 19

J. M. KRAFFT

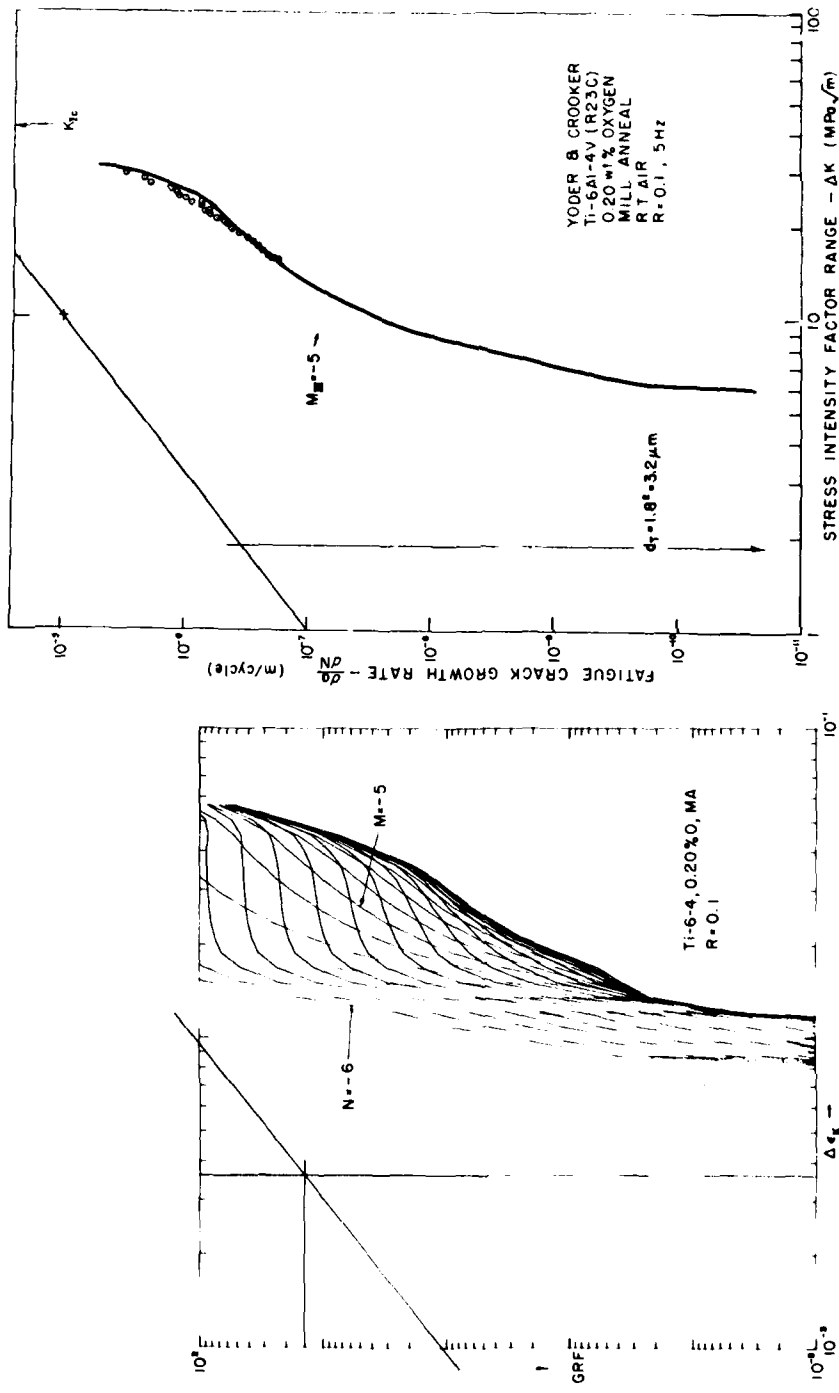


Fig. 22 — Growth-rate-factor curves for Ti-6Al-4V, 0.20% oxygen, mill anneal heat treatment, matched to air FCGR data of Yoder, Crooley, and Crooker. Ref. 18 and 19.

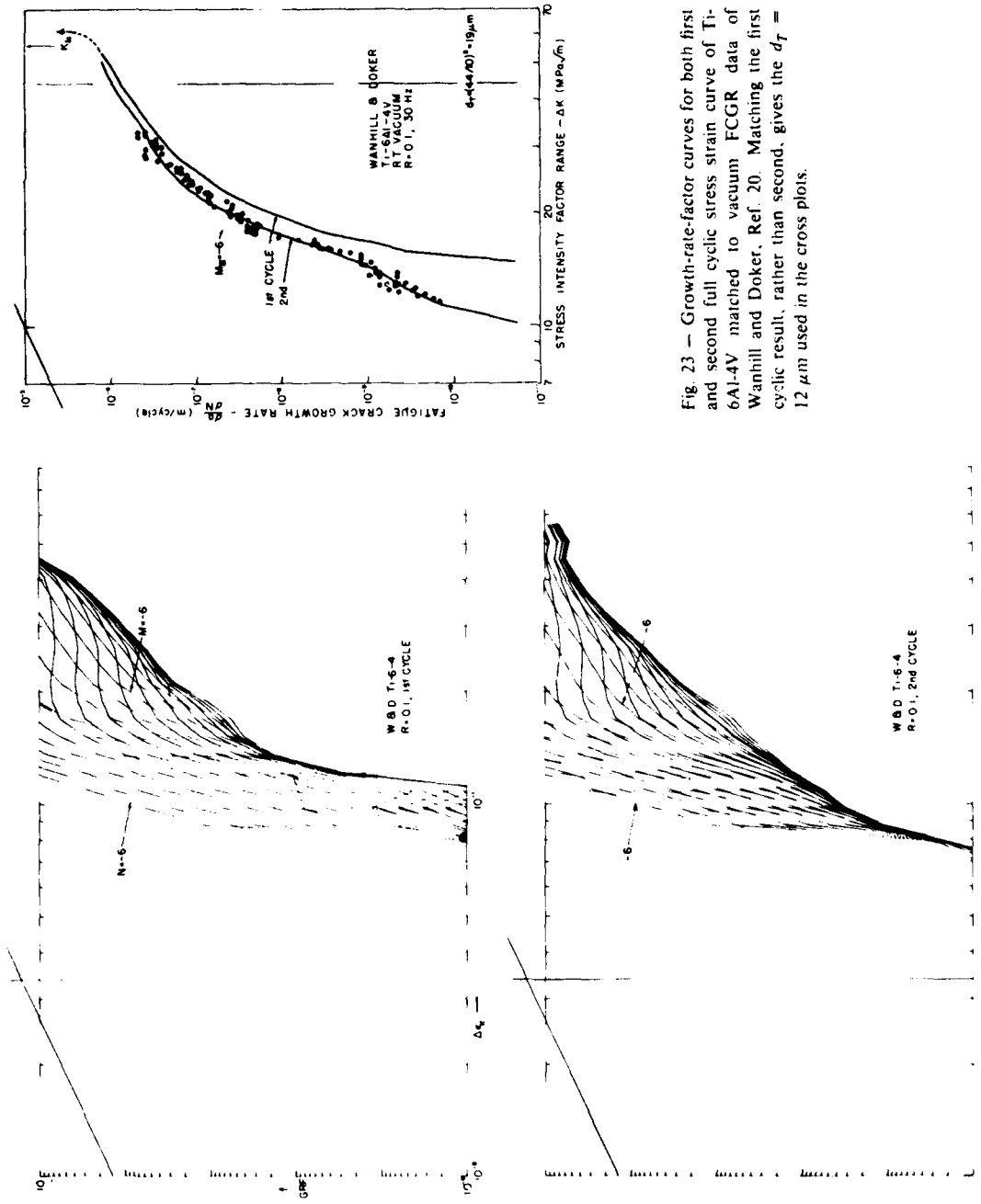


Fig. 23 — Growth-rate-factor curves for both first and second full cyclic stress strain curve of Ti-6Al-4V matched to vacuum FCGR data of Wanhill and Doker, Ref. 20. Matching the first cyclic result, rather than second, gives the $d_T = 12 \mu\text{m}$ used in the cross plots.

J. M. KRAFFT

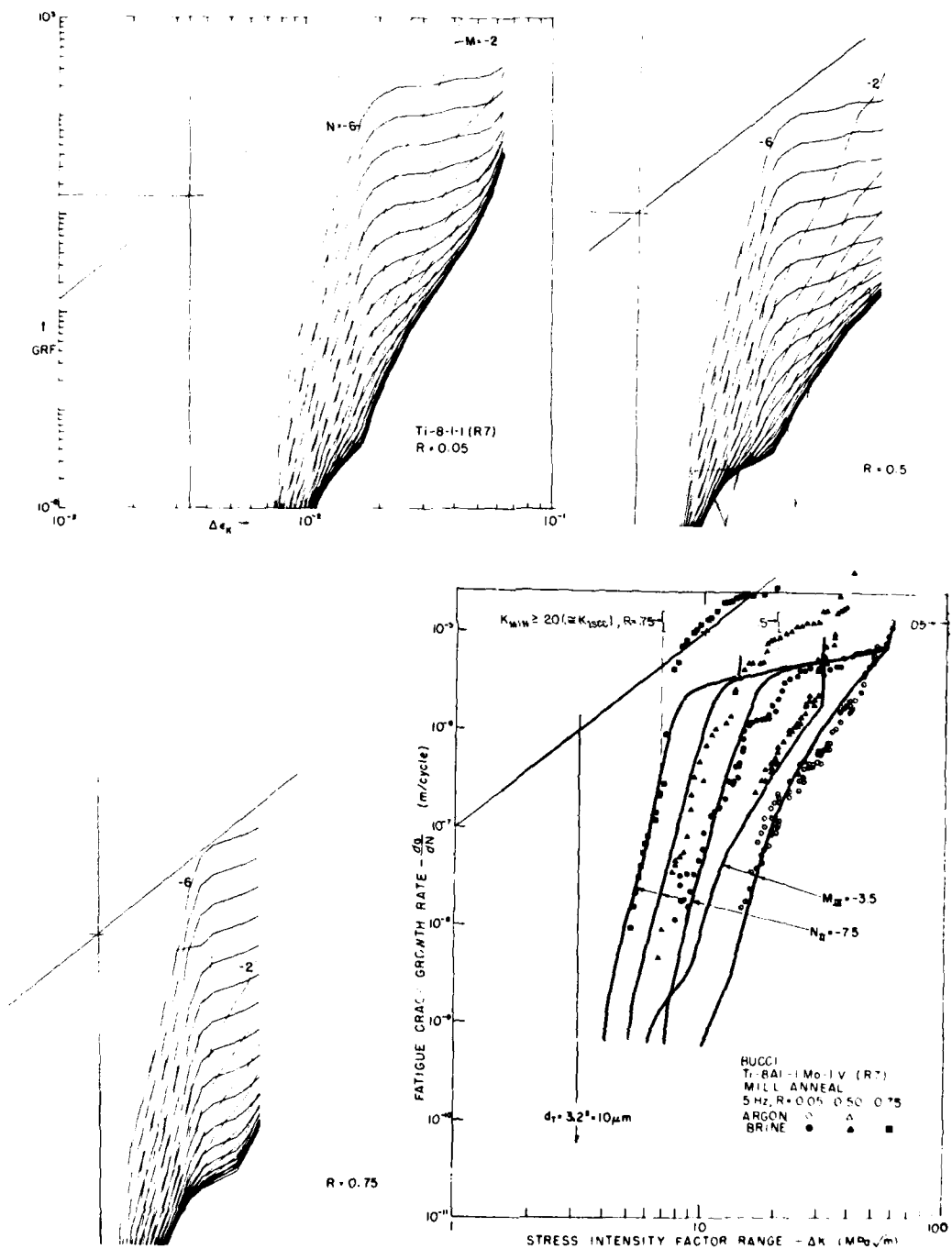


Fig. 24 — GRF curves for Ti-8Al-1Mo-1V, mill anneal, at three stress ratios is matched to argon and salt water data of Bucci, Ref. 21 and 22. Exceedance of actual rate at $R = 0.5$ and 0.8 is associated with region in which $K_{\min} > K_{f_{cr}}$.

NRL MEMORANDUM REPORT 4161

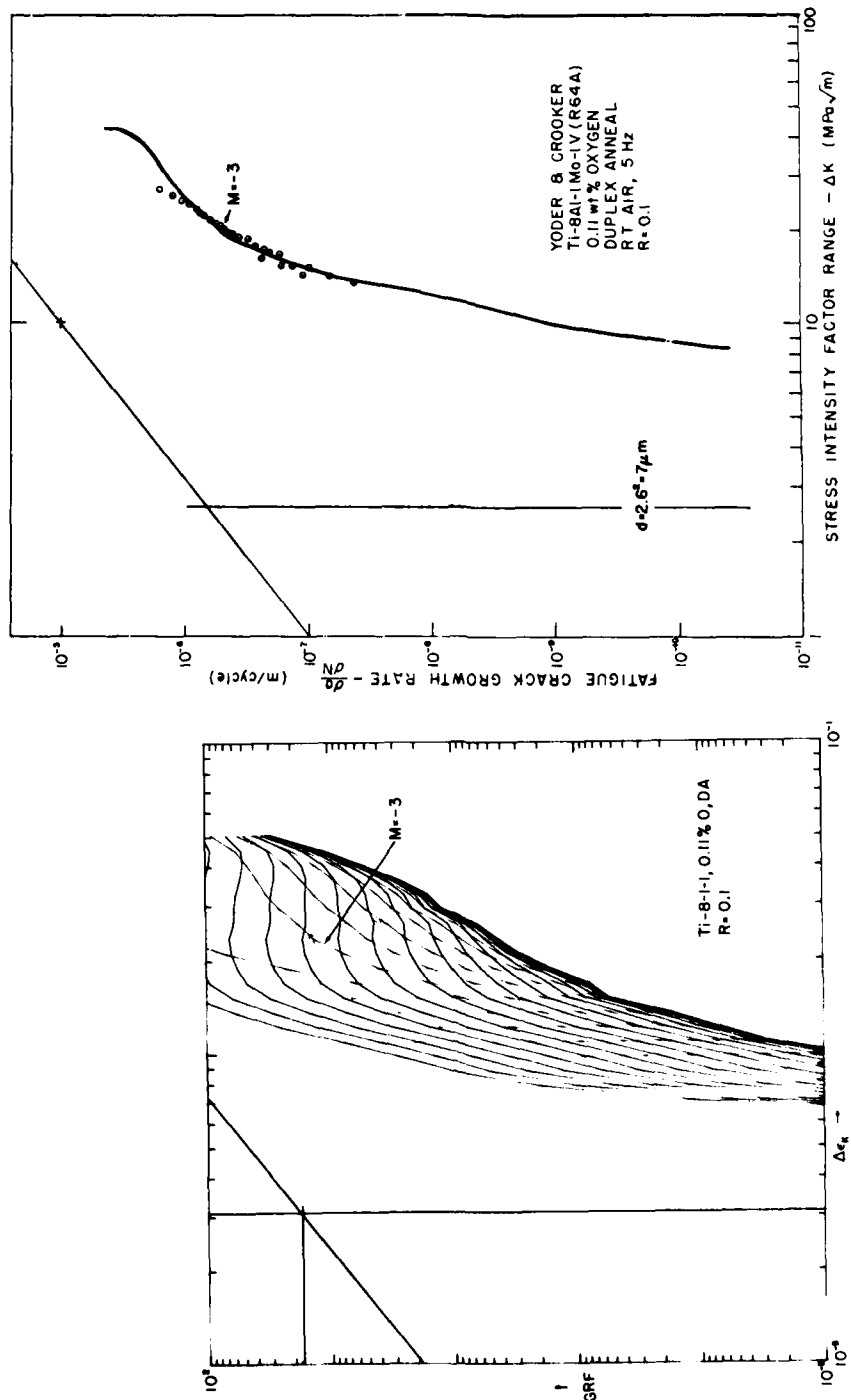


Fig. 25 — Growth-rate-factor curves of Ti-8Al-1Mo-IV, 0.11% oxygen, duplex anneal is matched to air FCGR data of Yoder, Cooley, and Crooker. Ref. 23 and 24.

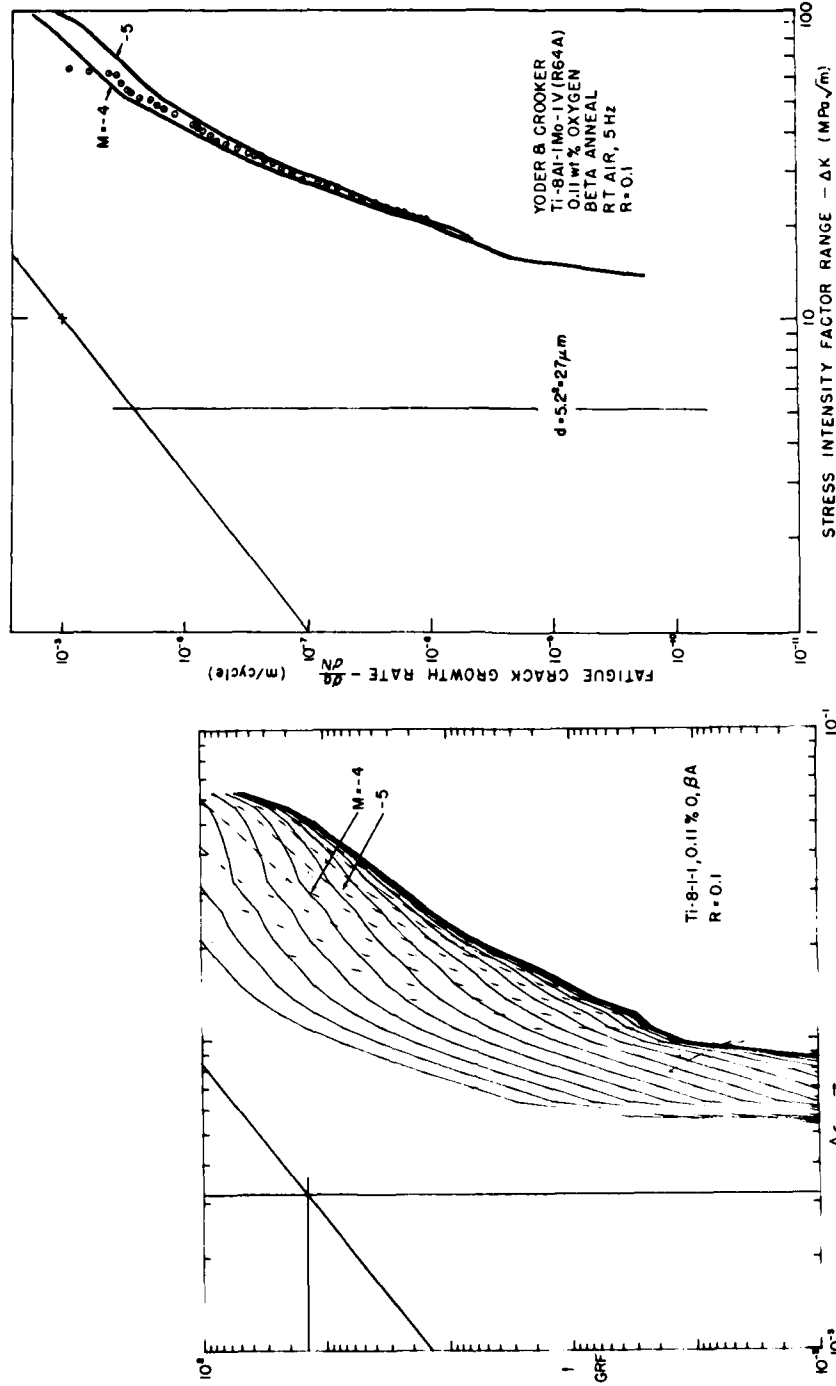


Fig. 26 — Growth-rate-factor curves of Ti-8Al-1Mo-IV, 0.11% oxygen, beta anneal heat treatment, is matched to air FCGR data of Yoder, Cooley, and Crooker, Ref. 23 and 24.

NRL MEMORANDUM REPORT 4161

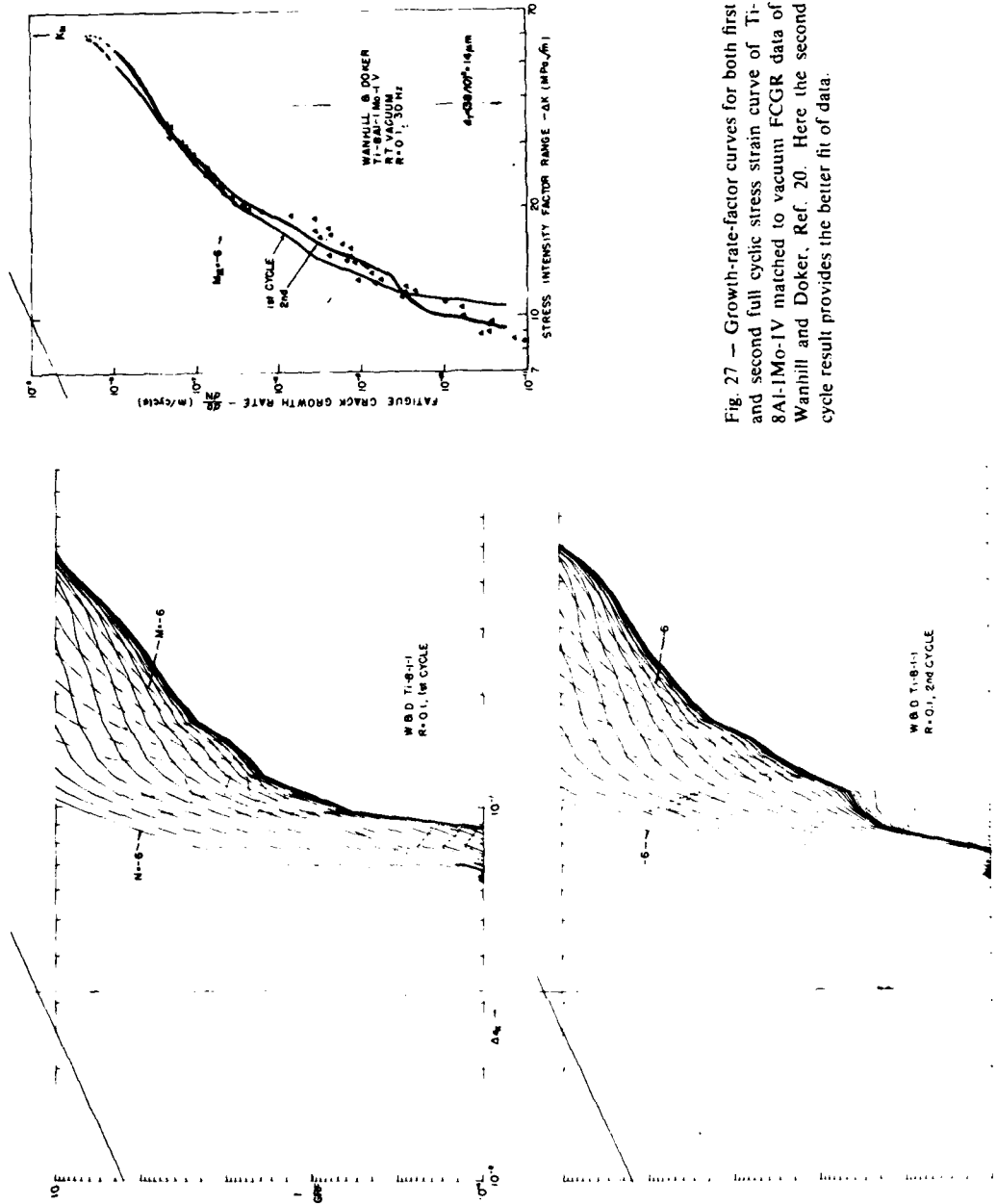


Fig. 27 — Growth-rate-factor curves for both first and second full cyclic stress strain curve of Ti-8Al-1Mo-IV matched to vacuum FCGR data of Wanhill and Doker, Ref. 20. Here the second cycle result provides the better fit of data.

Finally in the titanium alloys, results on the R-7 alloy used by Bucci is shown in Fig. 24. One need no longer be concerned that the growth rate in dry argon requires an M value comparable to those for room air environment. Later work of Wei and Ritter [31] show that minute traces of water could have caused this. The salt water data is nicely matched by $N_H = -7.5$ up to the region in which K_{max} exceeds K_{Isec} , whereupon a marked acceleration is observed.

4.3. Aluminum Base Alloys

Figures 28 and 29 display TLIM analysis of the two aluminum alloys.

Regarding the 2124-T851 data, Fig. 28, the mid- to upper-range fit is fairly satisfactory. However the TLIM estimates fall well below measured rates in the threshold region. It is here, much as with the high strength steels, as though the closure strain is too large. In the 2219-T851, Fig. 29, the fit is better. In both alloys thin specimens were cut out of thick plates so it is unlikely that surface stresses due to quenching from solution anneal played a role in either case.

In the 2219 data plot, Fig. 29, an attempt has been made to model the data at stress ratio -1. It is argued that one effect of compressing a crack might be to overcome the resistance of crack closure. To simulate this in the TLIM, one can remove the closure strain term and run the calculational program with R set to zero. The resulting curve seems to fit the data rather nicely. In fact in the high ΔK region, the fit is better than for the $R = 0.1$ data, where the runout rates exceed the TLIM curve, and oddly, the $R = -1$ data trend.

In this data, only the positive part of the stress excursion is used to calculate ΔK , even though the minimum stress is negative. When the Sasaki et al data [13] is treated in this way (not shown in Figs. 7 and 8), the TLIM estimate is too far to the left, as though some of the closure strain term should have been retained. More work is needed on this subject.

NRL MEMORANDUM REPORT 4161

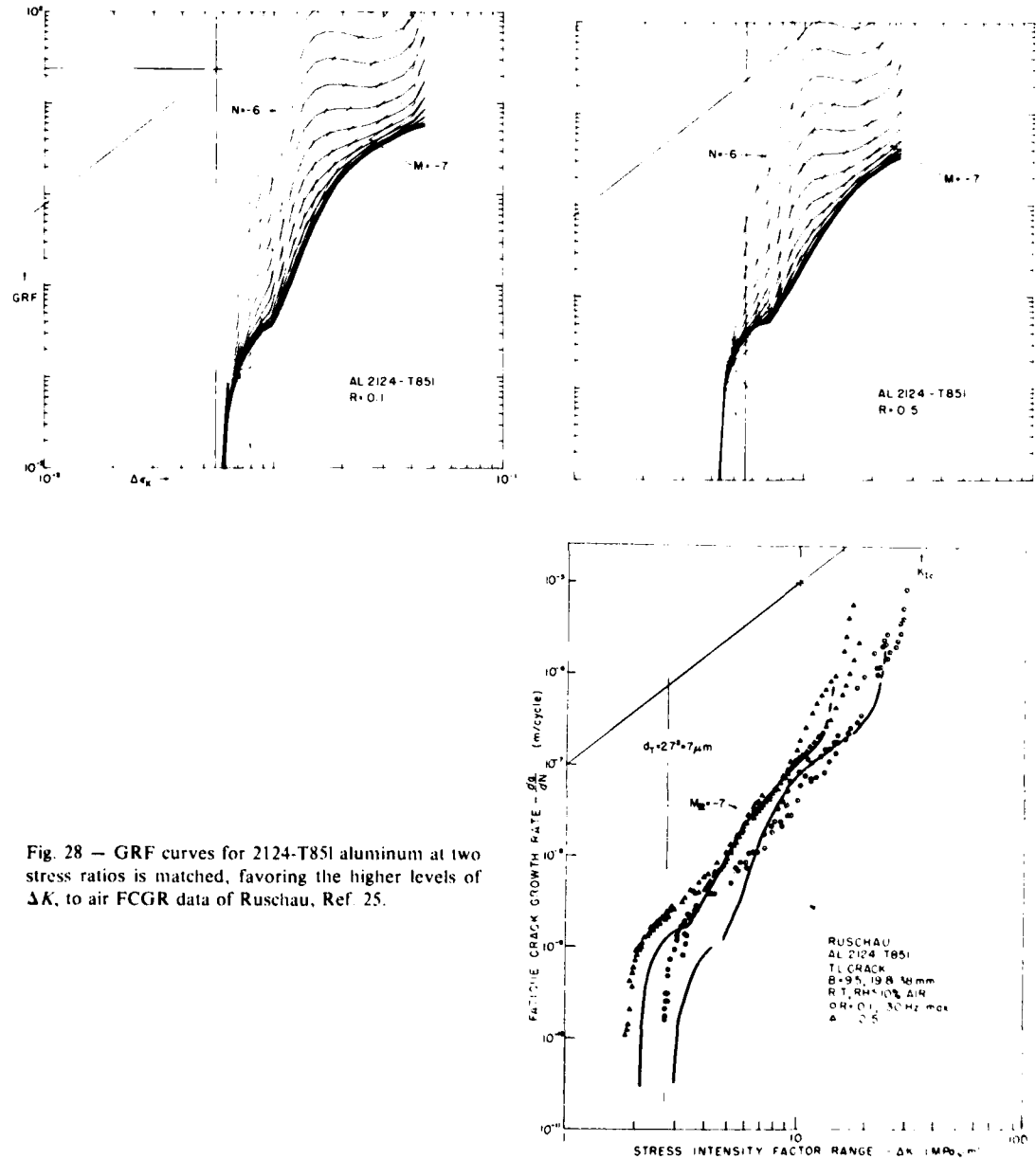


Fig. 28 — GRF curves for 2124-T851 aluminum at two stress ratios is matched, favoring the higher levels of ΔK , to air FCGR data of Ruschau, Ref. 25.

J. M. KRAFT

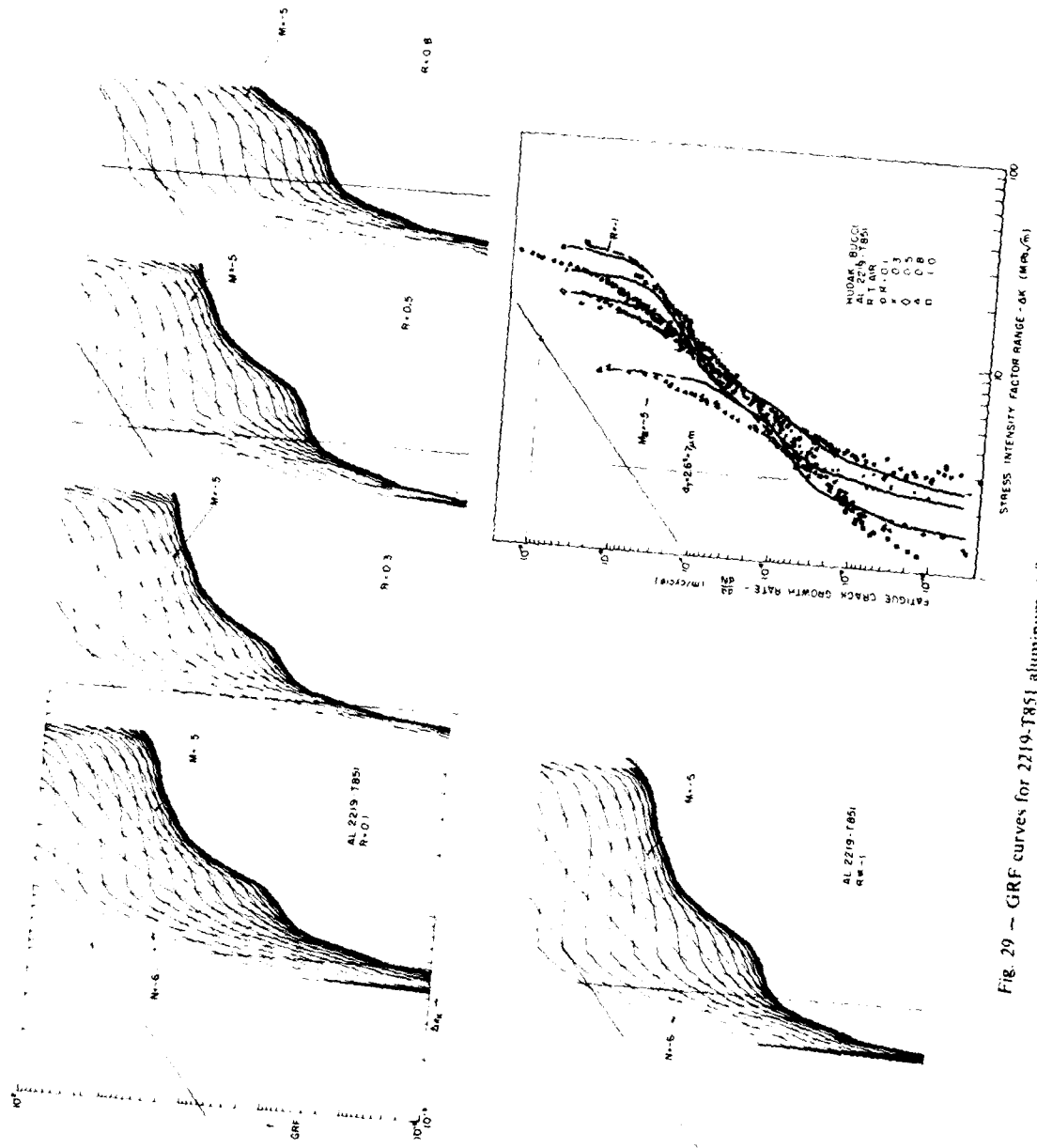


Fig. 29 - GRF curves for 2219-T851 aluminum at five stress ratios
data of Hudak and Bucci, Ref. 15.

5. COMPARISON OF FITTING PARAMETERS

It is suggested that the degree of correspondence between TLIM contours of fixed parameter designations and the fatigue crack growth rate data, Figs. 4-29, is encouraging. Some fits are extremely close; a few leave something to be desired, though not without extenuating circumstances. Since most of the correlations are close, it could be informative to consider implications of trends in fitting parameter values.

5.1. Trends in Process Zone Size

The process zone size is basic to the TLIM. It is required as a fitting parameter for every sort of environmental condition, including the dry inert gas or high vacuum. Indeed some sort of size parameter is generally necessary in any model relating flow properties to fracture behaviors. Recall here, that the process zone size is the distance ahead of the crack tip in the inverse square root strain singularity that provides the best-fit proportionality factor between measured strain in the tensile test, plus the closure strain, and ΔK or K_{Ic} in the fracturing test. The value, shown on each data match figure, is obtained from the intercept of the reference point $\Delta\epsilon_{KREF}$ on the ΔK scale. The square of this value of ΔK in MPa is d_T in $\mu\text{in.}$, as noted earlier.

Yoder has investigated effects of microstructural modification on FCGR in several Titanium alloys. He finds a substantial lowering of growth rate in mid-range with increase in effective grain size. In beta-annealed microstructures, grain size is identified with the Widmanstatten packet size whereas in lower temperature anneals it is associated with the alpha phase grain size. Heat treatments and average grain size values are given in Table II, and data matches leading to d_T in Figs. 17-23, 25 and 26. Fig. 30 is a (log) cross plot of the d_T process zone size against mean grain size of the titanium alloys. It shows a reasonable proportionality between the variables, perhaps a better correspondence with the process zone radius than its

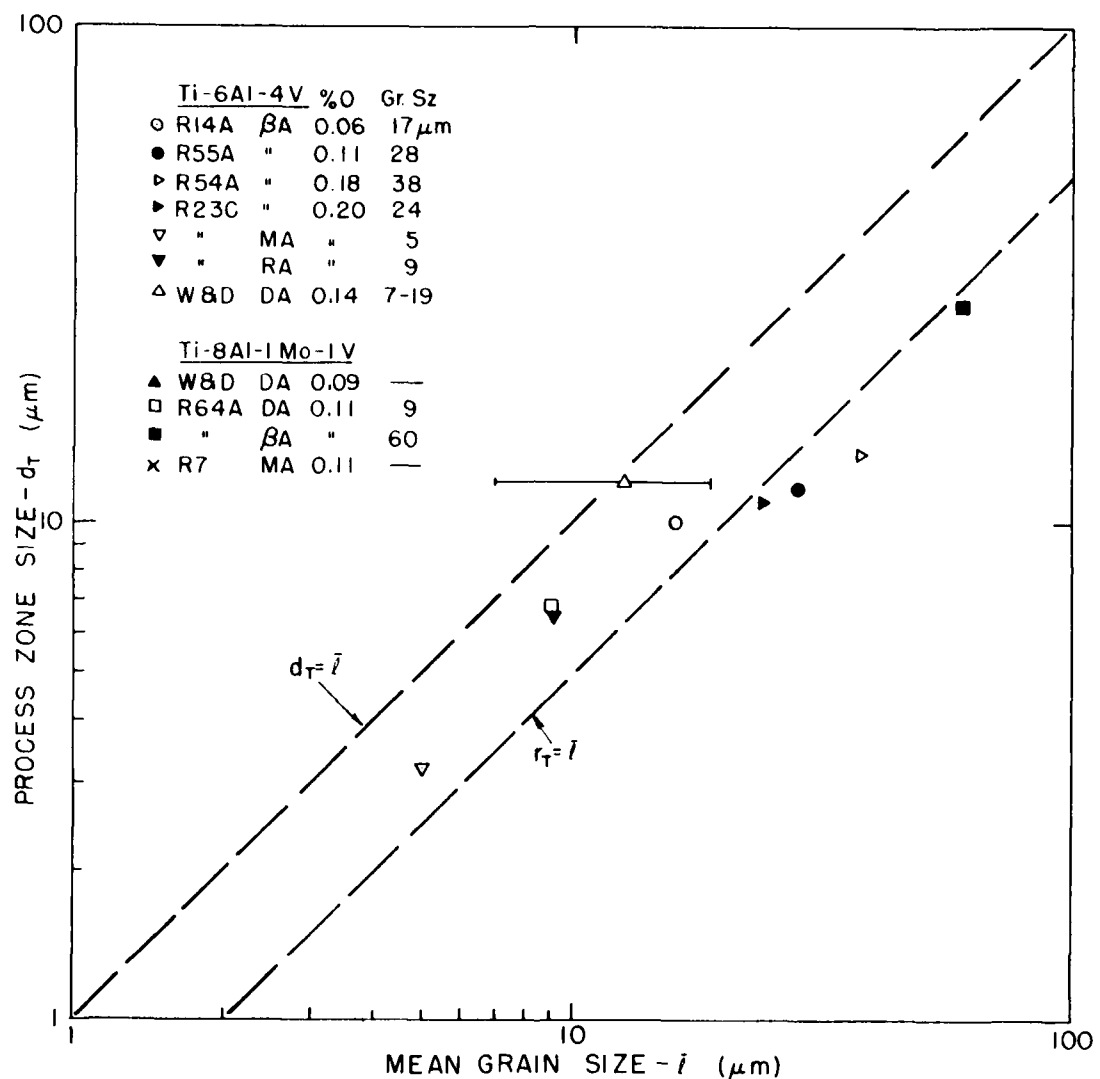


Fig. 30 — Cross plot of the process zone size matching parameter vs average grain size suggests a direct correspondence

diameter. This correlation suggests that one might associate the improvement in FCGR resistance due to a coarse microstructure to increased process zone size. Roughly speaking, if environmental factors are similar, increases in d_T transfer G values of a fitting TLIM curve along the match line direction, in ratio 2:1; e.g., a 20% increase in d_T increases growth rate by 20% percent but the ΔK to effect it is increased by 10%. If the slope of the log da/dN vs ΔK curve is greater than 2, as true of these alloys, the net effect is a decrease in growth rate for given ΔK . Some further decrease could result from changes in strength level as affecting the form of the stress strain curves. As noted earlier, the value of d_T for the Wanhill and Döker Ti-6Al-4V is that for a first full cyclic stress-strain curve, as is the case for all others, not the second cyclic curve which is matched in Fig. 23.

The correspondence of d_T with grain size suggests the plotting of it against yield strength, to which grain size is often related. Cross plots vs the 0.2% offset monotonic yield strength are shown in Fig. 31 for the steels and in Fig. 32 for the titanium alloys, in the uppermost data band. The process zone size in steel appears in steady decline with increasing yield strength. The slope of the band overlaid is as though a Hall-Petch relationship governed; i.e., d_T , via grain size, proportional to minus two power of yield strength, or a log slope of -2.

In the titanium alloys, the overlaid steel trend band from Fig. 31 seems to bound the data. However here, the trends do not suggest a -2 power slope. In the 6-4 data, increasing oxygen content increases yield strength with little effect on the d_T -value, as one might expect of an interstitial hardener. But the increase in yield strength with reduced d_T (hence grain size?) is far smaller than seen in the steels. Conversely, the loss of strength with improvements due increased d_T , is far less than might be feared. This lower sensitivity is also seen in the data on the 8-1-1 alloy on Fig. 32.

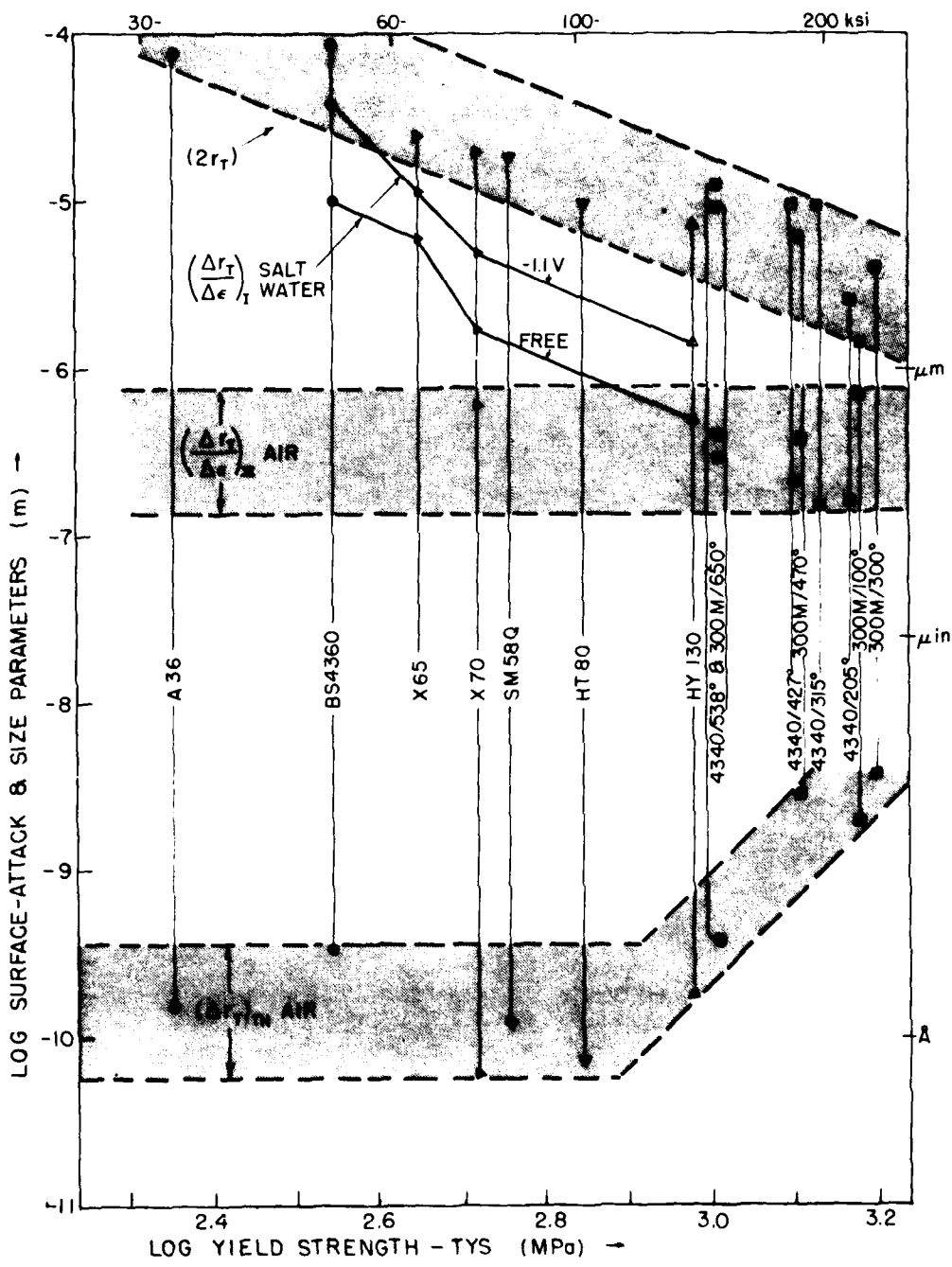


Fig. 31 — The size and surface-attack-depth values derived from TLIM matching of the various iron base alloys shows an internal consistency

NRL MEMORANDUM REPORT 4161

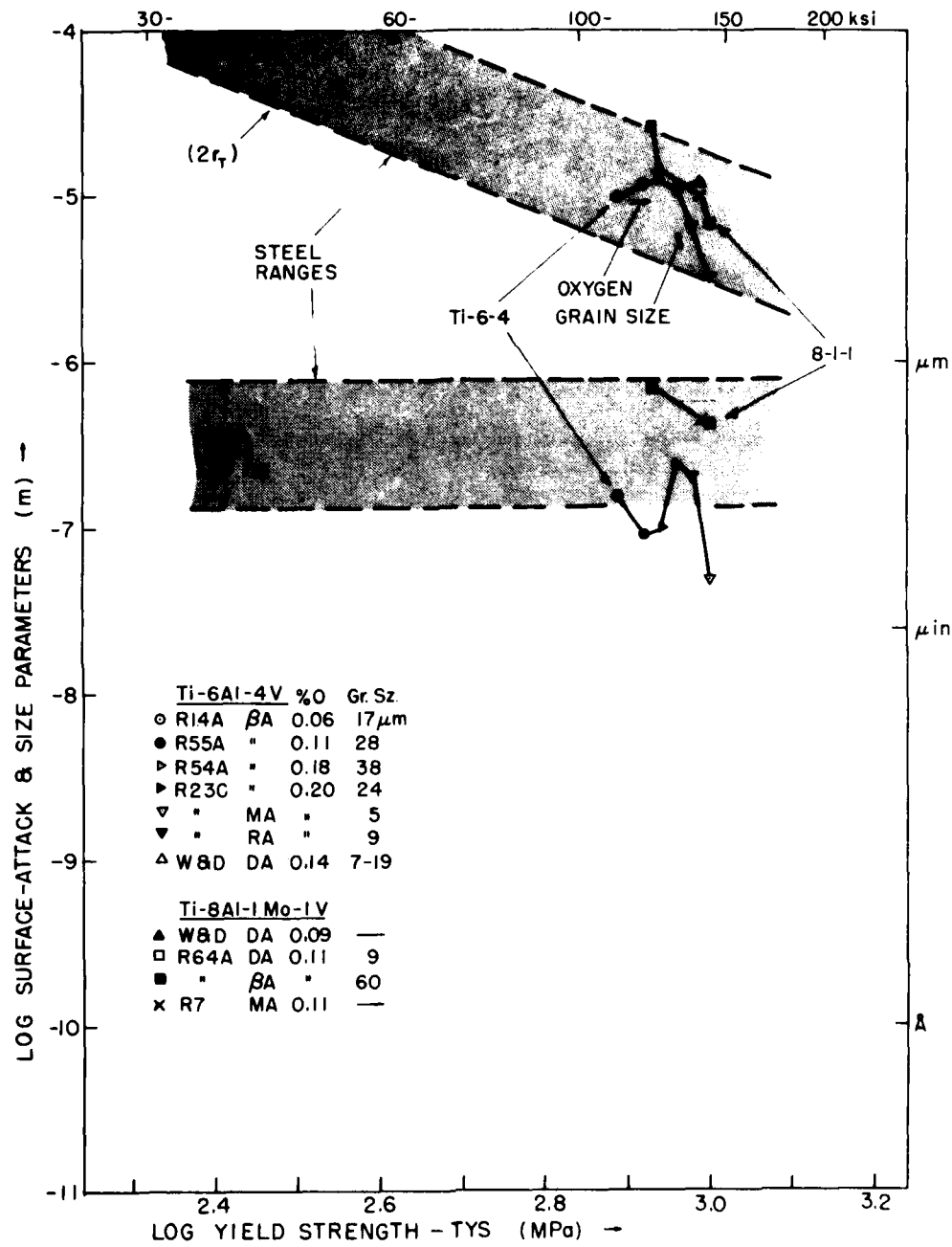


Fig. 32 — The size and surface-attack-depth values derived from TLIM matching of the various titanium base alloys.

5.2. Trends in Frequency-Independent Parameters

The normal frequency-independent parameters of the TLIM are two: the values of stage III strain-limited surface-attack M_{III} corresponding to air environment FCG; and characterizing stage-I aqueous environment CFCG M_I . In the sea-level air environment, adequate time for saturation of the surface attack process is thought, after results of Bradshaw and Wheeler [26], to be far shorter than any fatigue cycle. In the aqueous environments, the upper limit of stage I growth would normally be a function of cyclic frequency. It appears also that the threshold level of surface attack, N_{TH} or $(\Delta r_T)_{TH}$ also may be frequency independent, unlike stage II attack in corrosion fatigue, which is frequency dependent, as illustrated later.

Recall that values of these fitting parameters are obtained from the data match plots, where two to the N or M is the value of $[\Delta r_T/r_T]$ or $[\Delta r_T/r_T/\Delta\epsilon]$ respectively for the fit. Since the value of r_T is determined by fit location, the absolute value of Δr_T or $\Delta r_T/\Delta\epsilon$ is simply the product or 2^M times r_T . Such values as could be obtained are plotted vs yield strength for the air data in Figs. 31 and 32.

Values of $(\Delta r_T/\Delta\epsilon)_{III}$ are too small for determination in the softer steels. In these, the air data is essentially a G_2 -only match; negligible air-environment effect. However, in the higher strength 4340 type steels, Figs. 12-16, measurable values are discernible — of the order of 1/2 micron per unit strain.

The salt water environment, particularly at higher levels of impressed potential, does give measurable values of stage I strain-limited surface attack $(\Delta r_T/\Delta\epsilon)$, in the mild steels. Values are plotted in Fig. 31 for the extreme cases: free corrosion in -0.65V and closely coupled zinc potential, ≈ -1.1 V. These lie above the band laid over the air values, as expected. Unexpectedly, they indicate a downward trend with increasing yield strength, almost corresponding to

that for d_T . It is almost as though the relative surface attack $\Delta r_T/r_T/\Delta\epsilon$ is the more invariant parameter. The trend in $(\Delta r_T/\Delta\epsilon)_{III}$ air values also suggest this trend, but not so distinctly.

The residual attack $(\Delta r_T)_{TH}$, the lowest band in Fig. 31, appears only the order of a lattice spacing in the softer steels, rising some factor of ten for the hardest steels.

Regarding the titanium alloys, Fig. 31, stage III surface attack $(\Delta r_T/\Delta\epsilon)_{III}$ appears of similar severity to that for the steels but with the Ti-6-4 alloy definitely less susceptible than the Ti-8-1-1. No threshold data was available to permit estimate of $(\Delta r_T)_{TH}$ for these alloys.

5.3. Trends in Frequency-Dependent Parameters

The frequency-dependent parameter of the TLIM is the value of N , or corresponding Δr_T per cycle, fitting stage II corrosion fatigue growth region. Such values as are available in this collection are shown in Fig. 33. Here, on a logarithmic plot, the value of Δr_T is plotted against the loading time of the cycle. Using loading time rather than the half or full period follows the finding of Barsom [27] and of Kawai and Koibuchi [28] that this is the governing time in corrosion fatigue below K_{Isec} . Loading time is taken as 0.35 of cycle period for sinusoidal wave form and 0.5 for triangular, the latter form due to Vosikovsky. The slightly-tempered 4340 steels, M and N in Fig. 33, are also plotted this way even though the cycling is at a K_{max} generally exceeding the K_{Isec} threshold, for which a longer period fraction would be appropriate. In the case of the R-7 titanium of Fig. 24, the full-cycle period would seem warranted for the regions in which $K_{min} \geq K_{Isec}$.

In evaluating a plot as Fig. 33, one should place less confidence in the low values of Δr_T , as the small differences between M_I and M_{III} paths in this region make it difficult to fit. Also with small values of the environmental term, we should be in the transition region between

J. M. KRAFFT

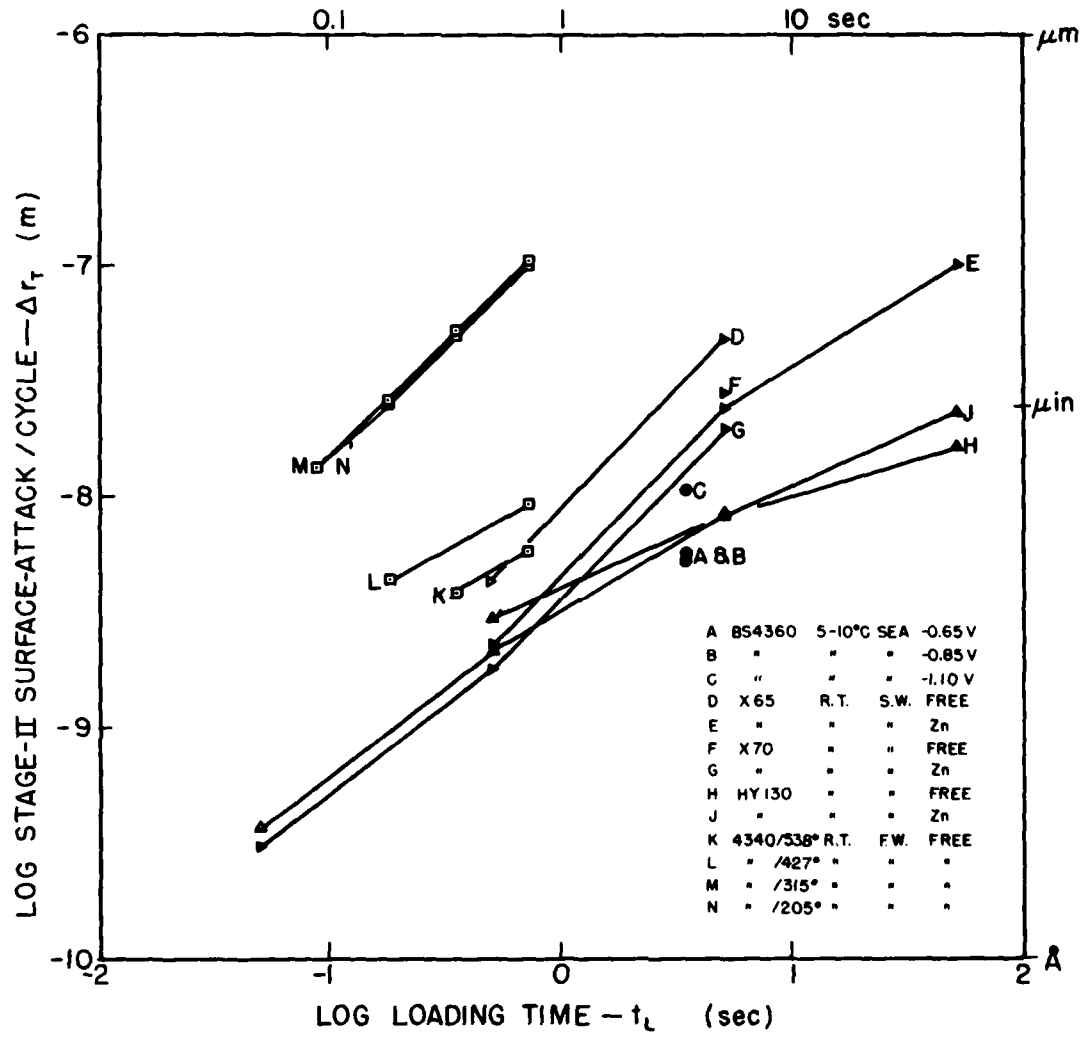


Fig. 33 — Values of the depth of surface attack in stage II growth derived from TLIM matching are plotted vs loading rise-time of the cycle.

cyclic and monotonic curve shape control, and the crudity of the abrupt transition algorithm could lead to inaccuracy. A slope of plus 1 on this plot would suggest a constant value of surface attack rate, called V_s in earlier papers. There appears to be a tendency for V_s to decrease with cycle period at longer cycle durations, presumably due to some sort of corrosion saturation effect.

6. DISCUSSION

A few caveats and generalizations are put forth in what follows.

6.1. Sources of Correlation Errors

There are, of course, at least two general sources: those of the modeling and those of the crack propagation data. The model is admittedly a primitive one. Its basic hypothesis, constant-load-at- d_T maintenance, can only be viewed as a possible necessary, but surely insufficient, condition. Properties of uniformly strained uniaxial specimens are applied to a region of high strain gradient and triaxial stress state. The characterizing tensile specimens are enormous compared to the zone of interest, which is in fact of the size scale of some of the strength affecting microconstituents. Indeed, if inclusions are stringerlike, this far exceeds the process zone size. The division of roles of monotonic vs cyclic properties is abrupt; the crack closure term rudimentary.

There are, additionally, errors of recording and measuring the stress-strain curves which can affect accuracy. The threshold determination is extremely sensitive to curve-shape around the proportional limit. The estimated points of fast fracture instability, or fatigue instability, is sensitive to curve shapes around maximum load. Aside from instrument errors, these things are affected by strain-rate and cyclic hardening/softening effects. The "two stage" hardening tendency in cycled titanium alloys is of concern.

Regarding errors in growth rate data, as sophistication in FCG measurements grows, more sources of data variability are being discovered. False thresholds pervade the literature — hopefully none in the data used here. Work by Crooker and Sullivan [29] show large effects of residual stress in the specimen. Actually, standard ASTM methods for FCG measurement are only now being issued. Thus it is not alone the model imperfections which must underlie all discrepancies.

6.2. d_T vs Microstructural Sizes

The 1967 work of Birkle, Wei and Pellissier [32] associated the d_T process zone size with the average spacing of largest inclusions of manganese sulfide in 4345 steel. Thus it is somewhat unexpected that the present results on titanium alloys, and by strong inference, those on structural steels, indicate an association with average grain size. In the titanium alloys, inclusions could hardly be a factor, as few, if any, are present. It is possible that in very fine grained materials, such as quenched and tempered 4345, control of the process zone size shifts from grain size to a coarser microconstituent such as the inclusions. Further work is needed here.

6.3. d_T from Low Temperature $K_{Ic}(K)$ Matchings

Another conflict with earlier concepts is in the magnitude of d_T values. Typically here for structural steels, d_T values from 10 to 100 microns are required for matching. Yet in extensive low temperature matching of the isothermal strain hardening exponent, or strain for maximum load, with plane strain fracture toughness, values on order of magnitude smaller were found [33]. It is clear that the latter values are too small to explain the room temperature fracture toughness of steels. One possible explanation is that low temperature toughness is to be associated with the adiabatic strain hardening rate, much lower than isothermal at the reduced specific heats of cyrogenic temperatures. Here although the process zone would be isothermally

quenched for any feasible crack loading time, the existance of an instability path to trigger a lower energy cleavage propagation leaves a choice. Given the general perversity of nature, and the unstable nature of crack propagation, the option for the easier path for fast fracture initiation is within the realm of possibility.

This concept poses a problem at temperatures/loading rates for which shear rather than cleavage processes characterize the separation. For example, in some aluminum alloys, fracture toughness actually rises at cryogenic temperatures [34] as does the isothermal strain hardening exponent, yet the decline of specific heat is not atypical for this metal.

An alternate to the constant d_T concept is, after Hahn et al [35], is a process zone limited by intercleavage facet ligamentary material to a size much smaller than that of the whole grain. Then in the transition to shear-dominated fracture, some sort of a transition in microseparation mode occurs, shifting the process zone size to control by grain size. Spitzig [36] supports an explanation of this sort.

6.4. Cleavage in FCGR Prediction

One should be cautious in attempting to use the TLIM for FCGR predictions when cleavage is included in the fracture process. This model implicitly assumes a ductile tear type instability as a local process. The additional growth due to local bursts of cleavage are seen by Stonesifer [37] and Richards and Lindley [38] to accelerate the average crack propagation rate. The TLIM, as presently constituted, has no way of accounting for this.

Stonesifer finds the fatigue upper limit K_{fc} to drop toward the threshold lower limit as temperature is reduced. He associates this with the drop in K_Ic with decreased temperature. Since this is cleavage fracture, the level of K_Ic cannot be predicted from non-cleavage values of d_T , as discussed in section 6.2, except possibly as an adiabatic initiation trigger.

While cleavage fracture is not handled here, the model does seem to provide useful correlations in regimes of FCG characterized by a variety of other non-cleavage fractographic features. For example, near the growth threshold, fracture surfaces can be characterized by almost planar separation, sometimes modulated by waves of minute striations. Scant evidence here of the d_T ligament such as the ductile tear dimple.

6.5. Yield Strength Effect on K_{TH} ; on K_{Ic}

The model algorithm permits a direct estimate of the threshold for FCG. In the non-vacuum environment, it is proportional to the monotonic yield point strain, from Eq. (26) and (29) approximately

$$\Delta K_{TH} = (1.5 - R) TYS \sqrt{2\pi d_T} \quad (37)$$

This is a slight overestimate, as the program detects the proportional limit, rather than 0.2% yield stress. Present results for steels, Fig. 31, show a decline in d_T with yield strength, approximately as inverse two power. Substituting an average line of this slope in Eq. (37) reduces it to

$$\Delta K_{TH} = (1.5 - R) \times 6.3 (MPa\sqrt{m}) \quad (38)$$

This suggests a trend of ΔK_{TH} from about 9 to 3 MPa \sqrt{m} as R varies from zero to plus one, independent of yield strength. This is in rough accord with literature data [39,40].

The effect on K_{Ic} , however, is not independent of yield strength. The model equates K_{Ic} to a product of the tensile instability strain and root of process zone size. In mild steels, the former tends to vary inversely with yield strength level and, as noted above, the latter also. From this, one would expect K_{Ic} to decrease markedly as yield strength increases. This is common knowledge, for example, the general character of trend lines of the Pellini ratio analysis diagram [42]. However, this argument, via association of d_T with grain size, also implies a K_{Ic} increasing with grain size. This is contrary the trends found by Stonesifer and Armstrong [42],

using prior austenite grain size in a pressure vessel steel. Perhaps using the grain size after heat treatment would reconcile this inconsistency?

6.6. Strain Rate Effects

Inasmuch as testing strain rate affects the stress-strain curve, it also influences growth rate factors of the TLIM. For best record precision, our tests are run at a slow head speed, giving a constant-load strain rate of about 10^{-3} sec $^{-1}$; test-fixture compliance markedly retards this in regions of high tangent-modulus. With this, a 5% strain excursion would require about 10^2 seconds. Typical cycle durations in fatigue tests are a factor of 10 to 1000 shorter than this.

Increased strain rate increases the elastic part of the flow stress. It will also affect the strain hardening rate. After Beeuwkes [43], body-centered-cubic steels will tend to be θ -invariant with strain rate. At strains near the proportional limit changes in strain and stress will tend to cancel, leaving the growth rate factor unaffected. At higher strains, the augmented stress will tend to increase GRF more than the elastic strain augmentation of total strain, thereby diminished percentage, will decrease it. However, the K -strain will be increased by the elastic strain augmentation, particularly on a log scale, in the low ΔK region. The net effect is to shift the da/dN prediction to the right at low to intermediate ΔK regions but to merge all frequencies at higher ΔK regions. The air fatigue data of Vosikovsky on X65 steel [11] indicates such a trend with cyclic frequency.

In the hexagonal titanium alloys, Beeuwkes sees a more moderate θ dependence on strain rate relative to σ . This would tend to reduce the augmentation of growth rate factor at mid- to high ΔK levels, producing a more continuous rightward shift of higher frequency data. Recent results of Chakrabortty et al [44] indicate such an effect.

J. M. KRAFFT

In the face centered cubic aluminum alloys, the strain rate sensitivity tends to be so low as to have little effect of this sort.

7. CONCLUSION

One would like to believe that the TLIM, as presently constituted, is ready for use. A number of "pros and cons" weigh in evaluation of its utility. On the positive side: it is firmly based on measured stress-strain data; it employs simple, limiting-case assumptions and hypotheses; it fits with parameters of minimum number, yet of physical implication; it embraces all aspects of FCG and CFCG from threshold to instability, and all environments including air and vacuum. On the negative side it is true that: the extra test for stress strain curves is burdensome; the analysis is primitive, verging on mere dimensional analysis; the fitting parameters are largely unverified by direct measurement; and in some cases, the TLIM fit is imperfect.

It is suggested that utility be judged in two separate applications. As a normalizing procedure for organizing FCGR data with a minimum parameter system, it would seem ready. In this use it should serve more effectively to focus the large ongoing effort in this field by providing a unifying basis for data comparison. The other application is in fatigue life prediction. Crack growth rate curves of maximum accuracy are needed for this, particularly in the threshold region. Here it would appear that in certain classes of structural materials, TLIM is of useful accuracy, hence could be employed. In others, more research is needed to determine whether this is feasible.

ACKNOWLEDGMENTS

The construction of the strain gage, production of the report, use of original data and helpful discussion by Mr. Curtis Lamb, Mrs. Barbara Bailey, Dr. Fred R. Stonesifer and Mr. Herschel Smith, respectively, is gratefully acknowledged.

REFERENCES

1. J.M. Krafft, "Strain-Hardening vs Stress-Relaxation Effects on Fatigue Crack Propagation," Report of NRL Progress, July 1971, p. 1-10.
2. J.M. Krafft, C.L. Lamb, and K.E. Simmonds, "Corrosion- and Creep-Induced Instability Modeling of Fatigue-Cracking in Various Alloys," NRL Memorandum Report 2399, February 1972. This and other NRL reports of this paper available from NTIS, Springfield, Virginia 22161, USA.
3. J.M. Krafft and H.L. Smith, "Ligament Instability Model for Stress Corrosion and Fatigue Crack Propagation in a 4340 Steel," Proc. Conf. Stress Corrosion and Hydrogen Embrittlement of Iron Base Alloys, Unieux-Firminy, France, (10-12 June 1973), NACE, Houston, 1977, pp. 482-494. See also NRL Memorandum Report 2598, April 1973.
4. J.M. Krafft and W.H. Cullen, Jr. "Organizational Scheme for Corrosion-Fatigue Crack Propagation," Engineering Fracture Mechanics, Vol. 10, 1979, pp. 609-650. See also NRL Memorandum Report 3505, July 1977.
5. R.W. Landgraf, "Cumulative Fatigue Damage Under Complex Strain Histories," ASTM-STP 519, 1973, p. 213-228.
6. J.G. Williams and C.E. Turner, "The Plastic Instability Viewpoint of Crack Propagation," Appl. Mat. Res. Vol. 3, 1964, pp. 144-147.
7. W. Elber, "Fatigue Crack Closure Under Cyclic Tension," Engineering Fracture Mechanics, Vol. 2, 1970, pp. 37-45.
8. L.F. Coffin, Jr. and J.F. Tavernelli, "The Cyclic Straining and Fatigue of Metals," Trans. Metals Soc. AIME, Vol. 215, 1959, pp. 794-807.
9. J.M. Krafft, "Application of the Tensile Ligament Instability Model of Crack Propagation to UKOSRP Data on BS4360 Grade 50D Steel," Proceedings ICM3, Cambridge, England, August 1979, pp. 383-396.
10. P.M. Scott and D.R.V. Silvester, "The Influence of Mean Tensile Stress on Corrosion Fatigue Crack Growth in Structural Steel Immersed in Sea Water," AERE Harwell, UKOSRP Report 3/02, May 1977.
11. O. Vosikovsky, "Fatigue Crack Growth In An X-65 Line Pipe Steel at Low Cyclic Frequencies in Aqueous Environments," Trans. ASME, J. Eng. Materials and Technology, Vol. 97, 1975, pp. 298-304.
12. O. Vosikovsky, "Effects of Stress Ratio on Fatigue Crack Growth Rates in X-70 Line Pipe Steel in Air and Salt Water," Canada Centre for Mineral and Energy Technology, Report EPR/PMRL 79-12 (J), February 1979.

J. M. KRAEFT

13. E. Sasaki, O. Ohta, and M. Kosugi, "Fatigue Crack Propagation Rate and Stress Intensity Threshold Level of Several Structural Materials At Varying Stress Ratios (-1 to 0.8)," *Trans. (Japan) National Res. Inst. for Metals*, **19**, 4, 1977, pp. 29-46.
14. O. Vosikovsky, "Frequency, Stress Ratio and Potential Effects on Fatigue Crack Growth of HY-130 Steel in Salt Water," Canada Mineral Research Program Report MRP/PMRI 77-6(J), May 1977, (27 pp).
15. S.J. Hudak, A. Saxena, R.J. Bucci and R.C. Malcolm, "Development of Standard Methods of Testing and Analyzing Fatigue Crack Growth Rate Data," Technical Report AFML TR 78-40, Wright-Patterson AFB, Ohio, May 1978.
16. R.O. Ritchie, "Influence of Microstructure on Near-Threshold Fatigue-Crack Propagation in Ultra High Strength Steel," *Metal Science*, Aug-Sept 1977, pp. 368-381.
17. G.R. Yoder, L.A. Cooley and T.W. Crooker, "Fatigue Crack Propagation Resistance of Beta-Annealed Ti-6Al-4V Alloys of Differing Interstitial Oxygen Content," NRI Report 8166, October 1977.
18. G.R. Yoder, L.A. Cooley and T.W. Crooker, "Enhancement of Fatigue Crack Growth and Fracture Resistance in Ti-6Al-4V and Ti-6Al-6V-2Sn Through Microstructural Modification," *J. Engineering Materials and Technology*, Vol. 99, 1977, pp. 313-318.
19. G.R. Yoder, L.A. Cooley and T.W. Crooker, "Quantitative Analysis of Microstructural Effects on Fatigue Crack Growth in Widmanstatten Ti-6Al-4V and Ti-8Al-1Mo-4V," *Engineering Fracture Mechanics*, Vol. 11, 1979, pp. 805-816.
20. R.J.H. Wanhill and H. Doker, "Vacuum Fatigue Fracture in Titanium Alloy Plate," NLR Netherlands Report MP 78002 U, December 1977.
21. R.J. Bucci, "Environment Enhanced Fatigue and Stress Corrosion Cracking of a Titanium Alloy Plus a Simple Model for Assessment of Environmental Influence of Fatigue Behavior," Ph.D. Thesis, Lehigh University, Bethlehem, Pennsylvania (1971).
22. Richard W. Hertzberg, "Deformation and Fracture Mechanics of Engineering Materials," John Wiley, New York, 1976, 605pp. (see Fig. 13.32)
23. G.R. Yoder, L.A. Cooley and T.W. Crooker, "Improvement of Environmental Crack Propagation Resistance in Ti-8Al-1Mo-4V Through Microstructural Modification," NRI Memorandum Report 3955, March 1979.
24. G.R. Yoder, L.A. Cooley and T.W. Crooker, "50-Fold Difference in Region II Fatigue Crack Propagation Resistance of Titanium Alloys, A Grain Size Effect," *J. Eng. Materials and Technology*, Vol. 101, 1979, pp. 86-90.
25. J.J. Ruschau, "Complete Fatigue Crack Growth Rate Curves for Aluminum Alloy 2124-T85 Including Typical Crack Growth Models," Technical Report AFML TR 78-155, May 1978.

NRL MEMORANDUM REPORT 4161

26. F.J. Bradshaw and C. Wheeler, "The Influence of Gaseous Environment and Fatigue Frequency on the Growth of Fatigue Cracks in Some Aluminum Alloys," Int. J. Fracture Mech. 5(4), 1969, pp. 255-268.
27. J.M. Barsom, "Effect of Cyclic-Stress Form on Corrosion- Fatigue Crack Propagation Below in a High-Yield Strength Steel," Proceedings, First International Conference on Corrosion Fatigue, Univ. of Connecticut, Storrs, June 1971.
28. S. Kawai and K. Koibuchi, "Effect of Waveform on Corrosion Fatigue Growth," Fatigue of Engr. Materials and Structures, Vol. 1, 1979, pp. 395-407.
29. A.M. Sullivan and T.W. Crooker, "The Effects of Thickness and Stress-Relief on Fatigue Crack Growth Rate in Ni-Cr-Mo-V Steel," J. Testing and Evaluation, Vol. 5, No. 2, 1977, pp. 96-101.
30. R.O. Ritchie, R.F. Smith and J.F. Knott, "Effect of Thickness on Fibrous Fracture From a Notch and on Fatigue Crack Propagation in Low-Strength Steel," Metal Science, Vol. 9, (1975), pp. 485-492.
31. R.P. Wei and D.L. Ritter, "The Influence of Temperature on Fatigue Crack Growth in a Mill Annealed Ti-6Al-4V Alloy," Journal of Materials, MJLSA, Vol. 7, No. 2, June 1972, pp. 240-250.
32. A.J. Birkle, R.P. Wei and G.E. Pellissier, "Analysis of Plane-Strain Fracture in a Series of 0.45C-Ni-Cr-Mo Steels With Different Sulfur Contents," Trans. ASM, Vol. 59, (1966) pp. 981-990.
33. J.M. Krafft, L.R. Hettche, A.M. Sullivan and F.J. Loss, "Fracture-Flow Relationships for A533B Pressure Vessel Steel," Trans ASME, J. Engineering for Industry, Vol. 92, Ser. B, (1970), pp. 330-338.
34. R.L. Tobler and R.P. Reed, "Fracture Mechanics Parameters for a 5083-O Aluminum Alloy at Low Temperatures," J. Eng. Materials and Technology, Vol. 99, Ser. H., No. 4, (1977) pp. 306-312.
35. G.T. Hahn, R.G. Hoagland, M.F. Kanninen, A.R. Rosenfield, and R. Sejnoha, "Fast Fracture REsistance and Crack Arrest in Structural Steels," Ship Structure Committee Report SCC-242, 1973.
36. W.A. Spitzig, "Correlations Between Fractographic Features and Plane-Strain Fracture Toughness in an Ultrahigh-Strength Steel.", Also, W.A. Spitzig, G.E. Pellissier, C.D. Beachem, A.J. Brothers, M. Hill and W.R. Warke, " A Fractographic Analysis of the Relationships Between Fracture Toughness and Surface Topography in Ultra-High Strength Steels," ASTM-STP 436, p. 17, (1968).
37. F.R. Stonesifer, "Effect of Grain Size and Temperature on Fatigue Crack Propagation in A533B Steel," Eng. Fracture Mechanics, Vol. 10, (1978), pp. 305-314.

J. M. KRAFFT

38. C.E. Richards and T.C. Lindley, "The Influence of Stress Intensity and Microstructure on Fatigue Crack Propagation in Ferritic Materials," *Engineering Fracture Mechanics*, Vol. 4, 1972, pp. 951-978.
39. L.P. Pook, "Fatigue Crack Growth Data for Various Materials Deduced from the Fatigue Lives of Precracked Plates," *Stress Analysis and Growth of Cracks, ASTM STP 513*, 1972, pp. 106-124.
40. O. Vosikovsky, "The Effect of Stress Ratio on Fatigue Crack Growth Rates in Steels," *Engineering Fracture Mechanics*, Vol. 11, (1979), pp. 595-602.
41. W.S. Pellini, "Criteria for Fracture Control Plans," *NRL Report 7406*, May 1972.
42. F.R. Stonesifer and R.W. Armstrong, "Effect of Prior Austenite Grain Size on the Fracture Toughness Properties of A533B Steel," *Fracture, 1977*, Vol 2, ICF4, Waterloo, Canada.
43. R. Beeuwkes, Proc. 3rd Sagamore Ordnance Research Conf., Syracuse University, New York, (1956), p. 89.
44. S.B. Chakrabortly, E.R. Starke, Jr., L. Konopasek and E.W. Lee, "The Effect of Environment and Frequency of Loading on the Fatigue Crack Propagation of Titanium-Vanadium Alloys," Proc. 3rd Intl. Conf. Mechanical Behavior of Materials, Cambridge, UK, August 1979, Vol. 2, pp. 365-370.